Systematic analysis of microtubule plus-end networks defines EB-cargo complexes critical for mitosis in budding yeast

Nikolay Kornakov[†] and Stefan Westermann[*]
Department of Molecular Genetics I, Faculty of Biology, Center of Medical Biotechnology, University of Duisburg-Essen, Universitätsstrasse 2, 45141 Essen, Germany

ABSTRACT **Microtubules are ubiquitous cytoskeletal polymers with essential functions in chromosome segregation, intracellular transport, and cellular morphogenesis. End-binding proteins (EBs) form the nodes of intricate microtubule plus-end interaction networks. Which EB binding partners are most critical for cell division and how cells organize a microtubule cytoskeleton in the absence of an EB protein are open questions. Here, we perform a detailed analysis of deletion and point mutants of the budding yeast EB protein Bim1. We demonstrate that Bim1 executes its key mitotic functions as part of two cargo complexes—Bim1-Kar9 in the cytoplasm and Bim1-Bik1-Cik1-Kar3 in the nucleus. The latter complex acts during initial metaphase spindle assembly and supports tension establishment and sister chromatid biorientation. We demonstrate that engineered plus-end targeting of Cik1-Kar3 and overexpression of the microtubule crosslinker Ase1 restore distinct aspects of the *bim1*Δ spindle phenotype. In addition to defining key Bim1-cargo complexes our study also characterizes redundant mechanisms that allow cells to proliferate in the absence of Bim1.**

Monitoring Editor
Kerry Bloom
University of North Carolina, Chapel Hill

Received: Feb 13, 2023
Accepted: Mar 2, 2023

INTRODUCTION

Microtubules are polar cytoskeletal filaments assembled from heterodimers of α- and β-tubulin. Their dynamics is described by non-equilibrium behavior in which individual filaments stochastically switch between phases of polymerization and depolymerization. This phenomenon, termed dynamic instability, is based on GTP hydrolysis of the β-tubulin subunit that poises filaments for disassembly. It also allows microtubules to explore the intracellular space efficiently and generate forces on cellular structures such as kinetochores and the cell cortex (Brouhard and Rice, 2018). The cellular functions of microtubules are controlled by microtubule-associated proteins (MAPs) that serve to regulate microtubule dynamics and organize microtubules into supramolecular structures such as the mitotic spindle. MAPs appear to have coevolved with tubulin and are already present in the last eukaryotic common ancestor (LECA) to regulate microtubule-dependent functions in the cell (Wickstead *et al.*, 2010). How tubulin polymers mediate DNA segregation and cell division has mostly been studied in eukaryotes, but homologous proteins are also present in bacterial phages and archaea (Yutin and Koonin, 2012; Fink and Lowe, 2015).

EB proteins are unique and particularly important plus end–interacting proteins (+TIPs) in eukaryotic cells (Schwartz *et al.*, 1997; Tirnauer *et al.*, 2002; Akhmanova and Steinmetz, 2008). Pioneering in vitro reconstitution experiments have revealed that EBs can localize to polymerizing plus-ends autonomously, that is, in the absence of proteins other than tubulin (Bieling *et al.*, 2007). They accomplish this by recognizing structural features unique to the GTP hydrolysis state of the microtubule, resulting in an increased residence time of EB molecules at the plus-end versus the microtubule lattice (Maurer *et al.*, 2012). Taking advantage of this property, EBs can recruit and enrich other proteins at plus-ends (Akhmanova and Steinmetz, 2008). Binding to EBs is established through protein–protein

This article was published online ahead of print in MBoC in Press (http://www.molbiolcell.org/cgi/doi/10.1091/mbc.E23-02-0054) on March 8, 2023.

[†]Present address: Laboratory of Chemistry and Cell Biology, The Rockefeller University, New York, NY 10065.

Author contributions: N.K. conducted all genetic, biochemical and live cell imaging experiments; N.K and S.W. wrote the manuscript; S.W. supervised the study and acquired funding.

Conflict of Interest: The authors declare no conflict of interest.

*Address correspondence to: Stefan Westermann (Stefan.Westermann@uni-due.de).

Abbreviations used: EB, end-binding; MT, microtubule; NES, nuclear export signal; NLS, nuclear localization signal; SPB, spindle pole body; +TIP, plus-end tracking protein.

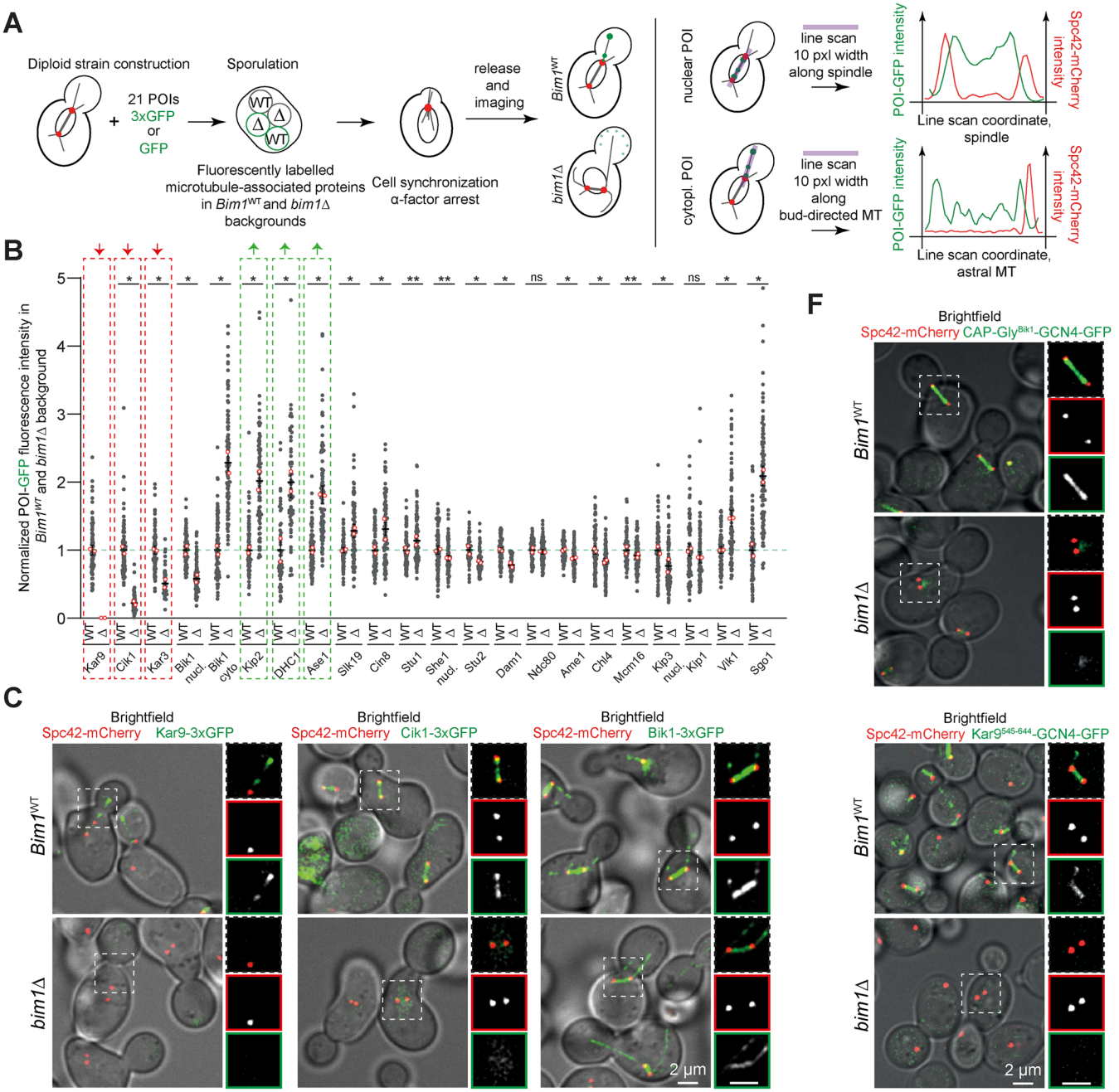
A
Diploid strain construction
21 POIs
3xGFP
or
GFP
Sporulation
WT
Δ
Δ
WT
Fluorescently labelled microtubule-associated proteins in Bim1WT and bim1Δ backgrounds
Cell synchronization α-factor arrest
release and imaging
Bim1WT
bim1Δ
nuclear POI
cytopl. POI
line scan 10 pxl width along spindle
line scan 10 pxl width along bud-directed MT
POI-GFP intensity
Spc42-mCherry intensity
Line scan coordinate, spindle
Line scan coordinate, astral MT
B
Normalized POI-GFP fluorescence intensity in Bim1WT and bim1Δ background
Kar9
Cik1
Kar3
Bik1 nucl.
Bik1 cyto
Kip2
DHC1
Ase1
Slk19
Cin8
Stu1
She1 nucl.
Stu2
Dam1
Ndc80
Ame1
Chl4
Mcm16
Kip3 nucl.
Kip1
Vik1
Sgo1
C
Brightfield
Spc42-mCherry Kar9-3xGFP
Spc42-mCherry Cik1-3xGFP
Spc42-mCherry Bik1-3xGFP
Spc42-mCherry Kar9545-644-GCN4-GFP
Bim1WT
bim1Δ
2 μm
F
Brightfield
Spc42-mCherry CAP-GlyBik1-GCN4-GFP
D
fragment with potential EB binding motifs
PBim1
POI
GCN4
GFP
Bim1-dependent MT binding
Affinity for Bim1
in vivo
in vitro (K´d, nM)
Bik1 1-100 CAP-Gly + 418 (279-634)
Kar9 545-644 SRIP LRPPTPL + 44 (37-51)
Ase1 701-798 SHIP +/- 1647 (?)
Ipl1 1-101 SKIP SKIP -/+ 1095 (?)
Duo1 197-247 THVP SGIP - Und
Ndc80 1-101 SQIP TGIP - Und
She1 161-259 LSKPKPF SSIP - NB
Bub1 361-460 SILP LAHETPV - not tested
Ctf3 72-122 LGTPTVF - not tested
E
POI on beads concentration (nM)
0 156 313 625 1250 2500 5000
0. GCN4
1. Bik1 1-100
2. Kar9 545-644
3. Ase1 701-798
4. Ipl1 1-101
5. Duo1 197-247
6. Ndc80 1-101
7. She1 161-259
Unbound Bim1 in supernatant, Mw~38 kDa

interactions between the EB-homology domain (EBH domain) and short linear interaction motifs (SLIMs) in the partner proteins (Honnappa *et al.*, 2009; Kumar *et al.*, 2017). Widespread EB binding motifs are SxIP, LxxPTPh, and combinations of these motifs (Buey *et al.*, 2012; Jiang *et al.*, 2012; Stangier *et al.*, 2018). Sometimes these motifs generate a sufficiently high binding affinity towards EB to enrich cargo proteins at plus-ends. It remains difficult to predict which protein may be a physiologically relevant binding partner of EBs in cells, as potential EB interaction motifs are present in many different proteins, generate only modest affinity to EBs and need to compete with many other proteins for a limited number of EB molecules in the cell. Moreover, extensive synthetic genetic interaction studies between deletion mutants have implicated Bim1, the only yeast EB protein, in a broad range of cellular processes (Tong *et al.*, 2001; Costanzo *et al.*, 2016). The phenotypes of the respective double mutants, however, have typically not been characterized in detail, making it difficult to assess the precise contribution of Bim1 to these processes.

Among the EB-interacting proteins, the CLIP-170 family of proteins (Bik1 in budding yeast) plays a distinct role. It uses a different binding mode to interact with EBs, via an N-terminal CAP-Gly domain that interacts with the carboxy-terminal aromatic residues of EBs (Stangier *et al.*, 2018). This interaction is sufficient to recruit CLIP-170 proteins to growing microtubule plus-ends (Bieling *et al.*, 2008). Because of this binding mode, Bik1 can participate in Bim1 complexes with other proteins and potentially modulate their functions (Moore *et al.*, 2006). It is, however, unclear which functions are executed by Bim1-Bik1 complexes in the cell, as opposed to functions that can be fulfilled by either partner independent of the other.

Here we take advantage of the reduced complexity of the microtubule network in *Saccharomyces cerevisiae* and the fact that this organism expresses only a single EB protein. As *BIM1* is a nonessential gene, the analysis of a microtubule cytoskeleton in the complete absence of an EB protein is possible. In addition, Bim1 mutants, specifically defective in different types of interactions with cargoes and Bik1, can be generated and analyzed. In this study, we set out to answer the following questions: Which microtubule-based processes are primarily affected by Bim1? What are the key Bim1 interaction partners in these processes, and which strategies do cells employ to organize the microtubule cytoskeleton in the absence of an EB protein? Our results indicate that artificial plus-end targeting of a single cargo, the kinesin-14 Cik1-Kar3, is sufficient to rescue most spindle-related *bim1* deletion defects in yeast cells. An increased accumulation of dynein–dynactin pathway components on the plus-ends of long astral microtubules helps to compensate for the absence of the Bim1-Kar9-Myo2 complex in spindle orientation. Our experiments define a minimal set of Bim1 cargoes needed to build and position a spindle for successful chromosome segregation.

RESULTS

A microscopy-based screen for Bim1-dependent microtubule localization in yeast cells

To fully define the contribution of Bim1 to cellular functions in yeast, we aimed to study systematically the consequences of a *bim1* deletion for the localization of a wide variety of proteins implicated in microtubule-related processes. To this end we rationally chose a collection of potential Bim1-binding proteins based on the following criteria: 1) reported involvement in the yeast spindle orientation pathways or nuclear spindle functions, 2) reported association with Bim1-Flag in IP-MS (van der Vaart *et al.*, 2017), and 3) predicted SxIP motifs or other putative Bim1-binding domains in unstructured regions, In addition, we confirmed that C-terminal tagging did not compromise the function of the tested proteins (Supplemental Figure 1A, Supplemental Table 1). In total, we tested 21 GFP or 3xGFP fusion proteins. To avoid cellular adaptation and accumulation of suppressor mutations, we constructed the GFP fusions in a hemizygous *bim1*Δ strain and imaged pairs of wild-type and *bim1*Δ mutants shortly after dissecting the diploids (Figure 1A). All GFP fusions were expressed to similar levels in wild-type and *bim1* deletion strains (Supplemental Figure 1B). Live-cell imaging was performed under standardized conditions for all strains following α-factor release from a G1-like state. The fluorescence intensity of the respective GFP-fusion was quantified along the spindle, or along a bud-directed cytoplasmic microtubule, respectively. The spindle pole body marker Spc42-mCherry was used to follow spindle morphogenesis (Figure 1A). Out of 21 GFP fusions, only two proteins fully depended on Bim1 for association with microtubules under these conditions (Figure 1B): the protein Kar9 in the cytoplasm and the Kar3 (Kinesin-14) partner protein Cik1 in the nucleus. Cik1 association with the spindle was nearly abolished in a *bim1*Δ mutant (Figure 1C), consistent with the finding that binding motifs in

FIGURE 1: A microscopy-based screen reveals the effects of a *bim1* deletion on a collection of microtubule-associated proteins. (A) Schematic overview of strain construction and quantitative imaging of selected proteins in *bim1* deletion cells (see details in *Materials and Methods*). (B) Overview of changes in microtubule localization to spindle or cytoplasmic microtubules of selected MAPs. Fluorescence intensity of the respective MAPs was normalized to one in the Bim1 wild-type strain. Small dots correspond to individual cells; open red circles represent mean values from two repeats. Error bars are mean values with 95% confidence intervals (CIs). More than 50 cells from two repeats were quantified for each condition. **, $p \leq 0.0001$; *, $p \leq 0.01$; $p \geq 0.05$; unpaired two-tailed Student's *t* test was used. (C) Selected examples for effects of *bim1*Δ on microtubule-associated proteins. Overlay of fluorescence microscopy with brightfield image on the left of every image. On the right side of every image, magnification of the boxed area is shown. From top to bottom: merged image, red channel, green channel. Scale bar, 2 µm. (D) Test for sufficiency of proposed Bim1 binding regions on the localization to microtubules in vivo and Bim1 binding in vitro. Selected fragments were cloned upstream of a GCN4 leucine zipper fused to GFP. For in vivo binding: +, localization to the spindle in all cells; +/-, most cells have signal above background; -/+, a few cells have a detectable signal; -, no localization observed. More than 100 cells from two repeats were examined. For in vitro binding, a dissociation constant with 95% CI is shown, calculated from three repeats. Labels: Und, undefined, for constructs whose dissociation constant is outside of the tested experimental range; NB, no binding. (E) Pull-down assay with immobilized GCN4 fusion constructs. Coomassie-stained samples showing Bim1 in the supernatant fractions of the pull down. (F) Examples of GCN4-GFP fusion proteins to the Bik1-, or Kar9- Bim1 interaction domains expressed from a *BIM1* promoter in wild-type or *bim1*Δ cells. Organization of the microscopy images as in C. Scale bar, 2 µm.

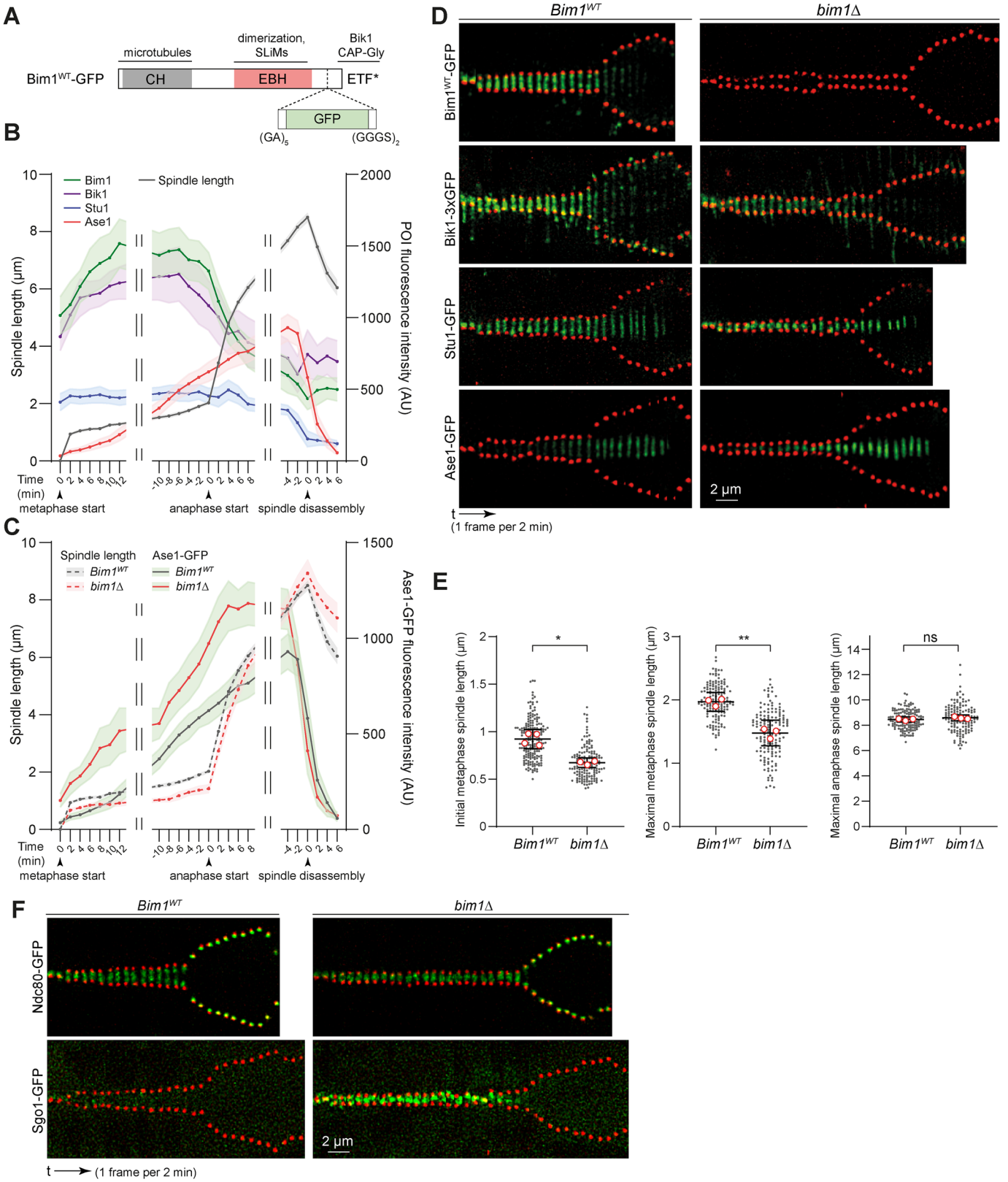

FIGURE 2: The spindle association dynamics of several MAPs is altered in *bim1* deletion cells. (A) Scheme for the construction of a functional Bim1-GFP fusion protein. GFP is inserted between the EBH domain and the extreme C-terminus. (B) Quantification of fluorescence intensity and spindle length as a function of time in wild-type cells. Start of metaphase, start of anaphase, and start of spindle disassembly are indicated in the graph; time (in minutes) is given relative to these reference points. Breaks in the graph are used to show correction for differences in metaphase and anaphase durations. Bim1, Bik1, Stu1, and Ase1 were quantified during spindle morphogenesis, from immediately after spindle pole body duplication until the start of disassembly of the anaphase spindle. For spindle size, 75 cells were

the N-terminus of Cik1 and Kar3 are necessary for the formation of a ternary Bim1-Cik1-Kar3 complex (Kornakov *et al.*, 2020). Spindle association of Kar3 itself was reduced, but not fully eliminated in the *bim1*Δ mutant, consistent with the formation of an alternative Kar3 motor complex with the Cik1 paralog Vik1, which localizes in a Bim1-independent manner to the spindle pole bodies (Manning *et al.*, 1999; Mieck *et al.*, 2015).

The deletion of Bim1 had differential effects on other spindle proteins: While the overall level of Bik1/CLIP-170 on the metaphase spindle was reduced by half, the association of other proteins, in particular the conserved cross-linking protein Ase1/PRC1, displayed a twofold increase (Figure 1B; Supplemental Figure 1C). The same trend was observed for other MT cross-linkers such as Slk19, the kinesin-5 family member Cin8, and the budding yeast CLASP homolog Stu1, which all showed a small but significant increase. For the kinetochore proteins tested in our collection, a slight reduction in their levels were observed for all subcomplexes, besides the major microtubule binding component of the kinetochore Ndc80 (Figure 1B; Supplemental Figure 1D). Reduction of Dam1c at the kinetochore upon Bim1 deletion was observed recently and has been attributed to the direct interaction between Duo1 and Bim1 (Dudziak *et al.*, 2021).

Upon analyzing the associations in the cytoplasm, we found that Kar9-3xGFP foci on bud-directed cytoplasmic microtubules were abolished in the *bim1*Δ strain, consistent with earlier reports (Miller *et al.*, 2000). Interestingly, the *bim1*Δ mutant had opposite effects on the microtubule association of Bik1-3xGFP in the cytoplasm versus in the nucleus: While the spindle association of Bik1 was reduced, the *bim1*Δ strain displayed a twofold increased level of Bik1 decorating long cytoplasmic microtubules (Figure 1, B and C). Bik1 appeared to be less confined to plus-ends, but instead could be detected in foci along the lattice, in line with previous observations (Stangier *et al.*, 2018). Along with Bik1, its binding partner, the plus-end directed kinesin Kip2 (Carvalho *et al.*, 2004), was also strongly enriched on cytoplasmic microtubules in the *bim1*Δ mutant. We conclude that only Kar9 and Cik1 strictly rely on Bim1 for microtubule association in cells and that *bim1*Δ mutants are characterized by long cytoplasmic microtubules strongly decorated with Bik1.

Fluorescent reporter constructs recapitulate Bim1-dependent binding in cells

The strict dependence of Kar9 and Cik1-Kar3 on the presence of Bim1, as well as the different effects of *bim1*Δ on nuclear and cytoplasmic Bik1, may reflect the formation of stable complexes between Bim1 and these binding partners in cells, as suggested from previous in vitro experiments (Manatschal *et al.*, 2016; Kumar *et al.*, 2021). To study whether Bim1 interaction motifs on selected candidate proteins are sufficient to recapitulate the localization of Bim1 cargoes in cells, we prepared constructs containing the predicted Bim1-binding regions dimerized by the Leucine-Zipper domain of GCN4 and fused to GFP (Figure 1D). We then asked if these constructs could directly interact with recombinant Bim1 in vitro. In parallel, we analyzed their localization in cells. Using quantitative pull-down assays, we found that the different constructs interacted with Bim1 with binding affinities decreasing in the order Kar9>Bik1>Ipl1≃Ase1>>others (Figure 1, D and E; Supplemental Figure 1E). The CAP-Gly domain construct, derived from Bik1 and expressed from a *BIM1* promoter, localized almost exclusively to the spindles of yeast cells. This localization was dependent on Bim1 (Figure 1F). This implies that other binding partners of the CAP-Gly domain, such as the carboxy termini of α-Tubulin (Tub1 and Tub3), are insufficient to localize this construct to the spindle or to cytoplasmic microtubules. We speculate that the CAP-Gly domain of yeast Bik1 has a much higher affinity to Bim1 (-ETF*) than to tubulin tails (-EEF*) within microtubules or, perhaps less likely, that tubulin tails are preblocked by other proteins in the cell. The Kar9 construct, on the other hand, localized to both cytoplasmic and spindle microtubules, and no microtubule association could be observed in a *bim1* deletion mutant (Figure 1F). Ase1 and Ipl1 constructs, which bind Bim1 with low micromolar affinity in vitro, were poorly recruited to spindles in vivo. Thus, strict dependence on Bim1 in cells correlates with a high affinity for Bim1-binding motifs in vitro.

Characterization of Bim1-dependent spindle phenotypes by live-cell microscopy

We next characterized the intranuclear phenotypes of *bim1*Δ cells by imaging spindle assembly in synchronized cells with 2-min time resolution. To visualize Bim1 itself, we constructed a new Bim1-GFP fusion (termed Bim1^{WT}-GFP) by inserting GFP with short linker sequences into the unstructured region between the EBH domain and the extreme C-terminus (Figure 2A). This construct avoids blocking the N- or C-terminus and in particular allows CAP-Gly domain-mediated binding of Bik1 to the C-terminal -ETF* motif of Bim1 (Stangier *et al.*, 2018). The construct fully rescued the temperature, hydroxyurea, and benomyl hypersensitivities of a *bim1*Δ mutant. In addition, Bim1^{WT}-GFP was able to support cell viability in the *mad1*Δ background, which lacks the spindle assembly checkpoint (SAC; Supplemental Figure 2A). Bim1^{WT}-GFP displayed a prominent spindle localization and a weak signal at the ends of astral microtubules. At both locations, Bim1 colocalized with Bik1, and on the spindle it colocalized with Stu2 (Supplemental Figure 2B). Using high–time resolution microscopy, we examined Bim1's behavior on dynamic microtubules in α-factor arrested cells. Bim1 tracked polymerizing and depolymerizing ends of cytoplasmic microtubule bundles as well as individual microtubules aligned along the bundles. Depolymerizing ends of individual microtubules were weakly stained with

analyzed. For fluorescence intensity, 20 Bim1-GFP, 15 Bik1-3xGFP, 15 Stu1-GFP, and 25 Ase1-GFP cells were quantified. Curves show mean values with 95% CIs. (C) Quantification of fluorescence intensity of Ase1-GFP (solid lines) and spindle length (dotted lines) over time on wild-type or *bim1*Δ spindles. Data for wild-type background are the same as in B. In the *bim1*Δ background, 25 cells were analyzed for spindle size and 15 cells for Ase1-GFP fluorescence intensity. (D) Representative reslices of selected GFP fusions throughout metaphase and anaphase of mitotic spindles in wild-type or *bim1*Δ cells. Images were scaled to equal intensity between wild-type and *bim1*Δ. Scale bar 2 µm, 1 frame/2 min. (E) Quantification of initial metaphase spindle length, maximal metaphase spindle length, and maximal anaphase spindle length for Bim1 wild-type and *bim1*Δ cells (*N* cells analyzed in every experiment: 200 and 150; 150 and 150; 150 and 135). Small dots correspond to individual cells; open red circles represent mean values of biological repeats. Error bars are mean values with 95% CIs. *, $p = 0.0014$; **, $p = 0.0013$; ns, not significant ($p = 0.1551$); unpaired two-tailed Student's *t* test was used. (F) Kymograph analysis of additional marker proteins Ndc80-GFP and Sgo1-GFP in wild-type and *bim1*Δ cells. Note high levels of Sgo1-GFP on metaphase spindle in the *bim1*Δ mutant. Scale bar 2 µm, 1 frame/2 min.

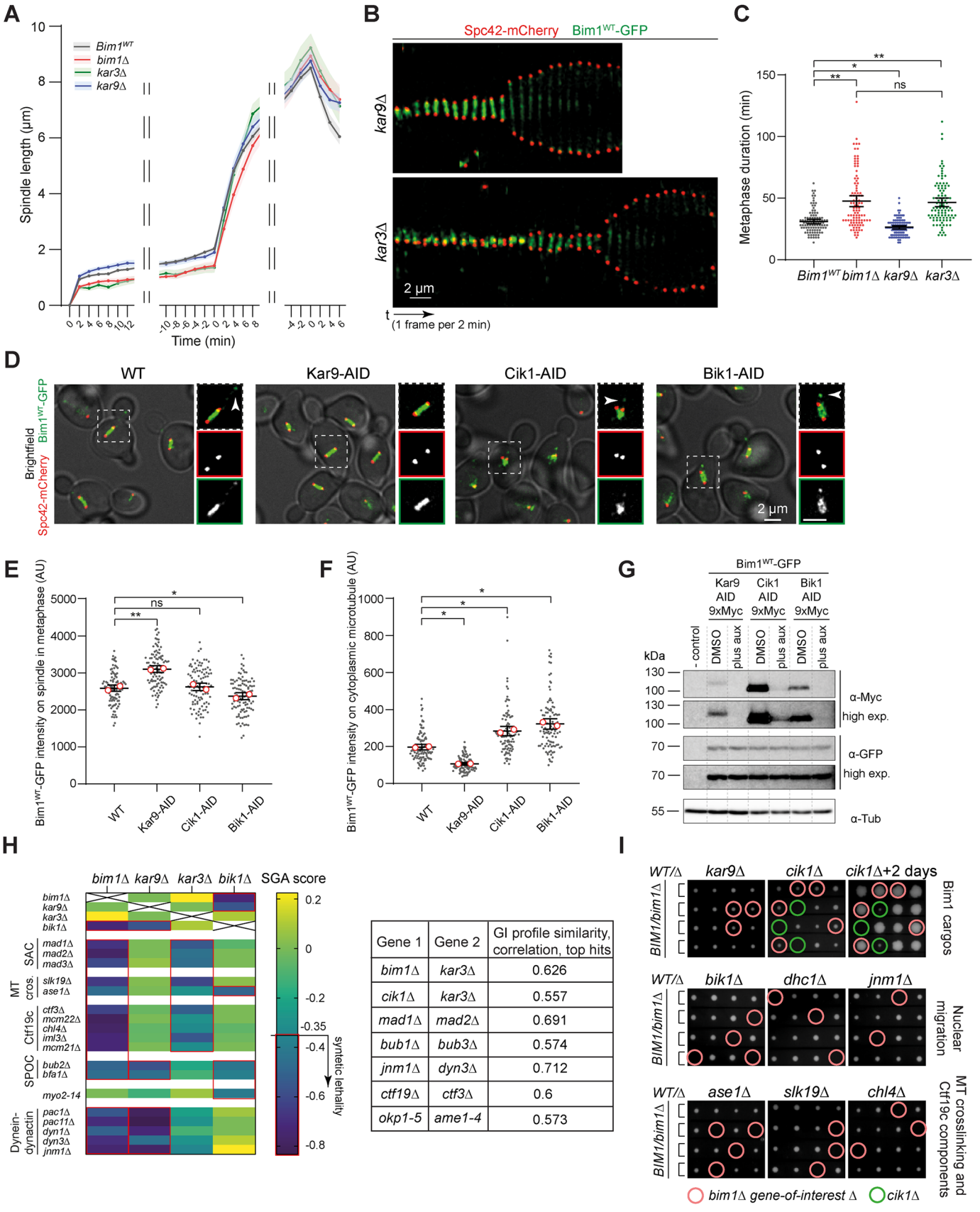

Gene 1	Gene 2	GI profile similarity, correlation, top hits
bim1Δ	*kar3Δ*	0.626
cik1Δ	*kar3Δ*	0.557
mad1Δ	*mad2Δ*	0.691
bub1Δ	*bub3Δ*	0.574
jnm1Δ	*dyn3Δ*	0.712
ctf19Δ	*ctf3Δ*	0.6
okp1-5	*ame1-4*	0.573

FIGURE 3: Bim1 executes its main nuclear function via the kinesin-14 Kar3. (A) Quantification of metaphase and anaphase spindle elongation kinetics in wild-type, *bim1Δ*, *kar9Δ*, *or kar3Δ cells*. Twenty-five spindles were analyzed for *kar9Δ or kar3Δ cells* (data for wild-type and *bim1Δ* cells are the same as in Figure 2C). Curves show mean values with 95% CIs. Note that metaphase spindle elongation profiles for *bim1Δ* and *kar3Δ* mutants closely resemble each other.

Bim1 (Supplemental Figure 2C). We then compared the association dynamics of Bim1 itself with that of other spindle MAPs. Bik1-3xGFP and Bim1^{WT}-GFP spindle association dynamics closely mirrored each other. Both proteins accumulated early on metaphase spindles, reached peak levels in the middle of metaphase, and declined upon anaphase onset (Figure 2, B and D; Supplemental Video 1). The remaining weak Bim1 and Bik1 signals in anaphase were localized at the spindle midzone, at kinetochore clusters, and at individual dots along the spindle (Supplemental Figure 2B). Consistent with the relatively low levels of Bim1 on anaphase spindles, parameters such as maximal anaphase spindle length, as well as anaphase spindle elongation kinetics, were largely unaffected in *bim1* deletion cells under our imaging conditions (Figure 2, C and E). In contrast to Bim1-Bik1, the level of the CLASP protein Stu1-GFP was relatively constant over time. The protein was present both on metaphase and anaphase spindles until spindle disassembly (Figure 2, B and D). Ase1-GFP was initially absent on the nascent metaphase spindle; its level then increased gradually until a maximum was reached shortly before anaphase spindle disassembly. Wild-type cells had 0.92 ± 0.06 µm initial metaphase spindle length, which gradually increased to 1.98 ± 0.07 µm before anaphase onset (mean ± SD). Cells lacking *BIM1* were characterized by shorter initial and maximal metaphase spindle lengths, 0.67 ± 0.02 µm and 1.48 ± 0.08 µm, respectively (Figure 2, C and E). Moreover, we found that metaphase spindle length typically increased monotonically in wild-type cells, whereas *bim1*Δ cells displayed more frequent fluctuations of metaphase spindle length over time (Supplemental Figure 2D). Abrupt changes in metaphase spindle length of *bim1*Δ cells were often associated with transient pulling and pushing events, when the spindle was tumbling between mother cell and bud (Supplemental Video 1 and 2). Similar behavior has previously been reported for *ase1*Δ and could be explained by dynein-dependent forces applied to astral microtubules connected to a spindle that is compromised in microtubule crosslinking (Estrem and Moore, 2019). Since we established that *bim1*Δ cells loaded much more Ase1 on their short spindles, we decided to investigate the timing of Ase1 recruitment. Surprisingly, we found that in *bim1*Δ cells Ase1 was already present at a detectable, albeit low, level before bipolar spindle formation (Figure 2C; Supplemental Video 1). As mitosis progressed, the Ase1 signal increased continuously and was higher than in wild-type cells during both metaphase and anaphase (Figure 2, C and D). In addition to Ase1, we followed the kinetochore proteins Ndc80-GFP and Sgo1-GFP, the latter of which specifically marks kinetochores that lack tension (Indjeian *et al.*, 2005). We observed that *bim1*Δ cells less frequently showed a bilobed Ndc80-GFP distribution on the metaphase spindle. These spindles were also characterized by a bright and persistent Sgo1-GFP signal that was much stronger than in wild-type cells (Supplemental Figure 2E; Figure 1B). This indicates that kinetochores in *bim1* deletion cells have problems forming tension-bearing attachments, which activates the mitotic checkpoint and prolongs metaphase.

Bim1 confers its major function for the metaphase spindle via the kinesin-14 motor Cik1-Kar3

Next we compared the *bim1*Δ phenotype to deletions of its main cargoes Kar3 and Kar9. Analyzing spindle elongation kinetics in the respective deletion strains showed that a *kar3* deletion indeed closely reflects the *bim1* deletion (Figure 3, A and B). *kar3*Δ spindles were initially shorter and had a decreased maximum metaphase spindle length, while metaphase duration increased to 47 ± 18 min (48 ± 22 min for *bim1*Δ and 31 ± 10 min in wild-type cells, mean ± SD; Figure 3C). Unexpectedly, the *kar9* deletion mutant displayed a slightly accelerated metaphase progression relative to wild-type cells (26 ± 7 min; Figure 3C). This may be attributed to an increased level of Bim1 on the metaphase spindle in the absence of Kar9, which in turn may facilitate an activity of a Bim1–cargo complex that could support biorientation (Figure 3, D and E). In this context, we noticed that cells acutely depleted of Kar9 (*Kar9-AID*) almost completely lack cytoplasmic Bim1 (Figure 3, D and F), while the overall level of Bim1 in Western blots was unchanged (Figure 3G). Thus, Kar9 and Bim1 are mutually dependent for their cytoplasmic localization and lack of Kar9 impacts the distribution of Bim1 between the cytoplasm and the nucleus. This finding supports a recently published model that proposes that nuclear–cytoplasmic shuttling of

(B) Kymographs of Bim1 association during metaphase and anaphase on spindles in a *kar9* and a *kar3* deletion. Note reduced metaphase spindle size in the *kar3*Δ strain. Scale bar 2 µm, 1 frame per 2 min. (C) Quantification of metaphase duration in the indicated strains. For each condition, 100 cells were quantified. Error bars are mean values with 95% CIs. **, $p < 0.0001$; *, $p = 0.0005$; ns, not significant ($p = 0.9841$); Welch and Brown-Forsythe ANOVA with Games and Howell post-test was used. (D) Effects of acute depletion of Kar9, Cik1, or Bik1 on the localization and distribution of Bim1. Fluorescence micrographs showing Bim1^{WT}-GFP and Spc42-mCherry in wild-type cells or upon acute depletions of Kar9, Cik1, or Bik1. Overlay of fluorescence microscopy with brightfield image at the left side of every image. On the right side of every image, magnification of the boxed area is shown. From top to bottom: merged image, red channel, green channel. Arrowheads point to Bim1^{WT}-GFP on cytoplasmic microtubules. Scale bar, 2 µm. (E) Quantification of Bim1^{WT}-GFP intensity on the metaphase spindle in wild-type or depletion strains. Note increased level of Bim1 on metaphase spindle upon depletion of Kar9. One hundred cells were analyzed for each condition. Error bars are mean values with 95% CIs. **, $p < 0.0001$; *, $p = 0.0019$; ns, not significant ($p = 0.9517$); Welch and Brown-Forsythe ANOVA with Games and Howell post-test was used. (F) Quantification of Bim1^{WT}-GFP intensity on the cytoplasmic microtubules in wild-type or depletion strains. One hundred cells were analyzed for each condition. Error bars are mean values with 95% CIs. *, $p < 0.0001$; Welch and Brown-Forsythe ANOVA with Games and Howell post-test was used. (G) Western blot showing effectiveness of depletion of Kar9, Cik1, and Bik1. Whole-cell extracts were separated by SDS–PAGE, blotted, and probed with anti-myc (AID-fusion) or anti-GFP antibody (Bim1). To enhance the Cik1 signal, α-factor arrested cells were used, which express elevated levels of Cik1. (H) (Left) Synthetic genetic analysis assigning SGA scores to combinations of deletion mutants. SAC, spindle assembly checkpoint; SPOC, spindle position checkpoint. Synthetically lethal interactions are concluded in the red box. (Right) Pearson correlation is shown for SGI profiles of selected genes. (I) Heterozygous diploid dissection of different gene deletions in a *bim1*Δ background. Four spores of a tetrad are displayed horizontally; the indicated genotypes are marked by circles. Note that *bim1*Δ *kar9*Δ and *bim1*Δ *cik1*Δ double mutants are viable.

Kar9 controls the cytoplasmic localization of Bim1 (Schweiggert *et al*., 2016) and is also in line with the finding that oligomerization of Kar9 is required for the formation of a tight complex with Bim1 (Kumar *et al*., 2021). Cik1 depletion had no detectable effect on the amount of Bim1 on the spindle, but instead caused increased recruitment of Bim1 on astral microtubules (Figure 3, D–F). Loading of Bim1 on the spindle was partially dependent on Bik1. Bik1 depletion led to a coordinated decrease in nuclear and increase in cytoplasmic Bim1, and cytoplasmic microtubules were very short in the absence of Bik1 (Figure 3, D–F). Overall, our cell biology data suggested that major nuclear Bim1 functions are conducted in a complex with Cik1-Kar3.

To relate these cell biological observations to genetic data, we compared the genetic interaction profile of a *bim1* deletion with that of various other factors by reanalyzing the synthetic genetic interaction data from Costanzo *et al*. (2016) and TheCellMap.org Usaj *et al*., (2017). A comparison of the genetic interaction profiles shows that a *kar3* deletion was most similar to a *bim1* deletion, while a *kar9* deletion resembled the *bim1* deletion profile only with regard to mutants in the dynein–dynactin complex (Figure 3H). Quantitative correlation between genetic interaction profiles of *bim1*Δ and *kar3*Δ was in the same range as for members of established multiprotein complexes, such as Bub1-Bub3, Mad1-Mad2, or the centromere-associated proteins Ctf19 and Ctf3 (Figure 3H). If Bim1 confers its functions indeed in the form of Bim1-Cik1-Kar3 complexes in the nucleus and Bim1-Kar9 complexes in the cytoplasm, then combinations of the respective deletion mutants should not show synthetic defects, but might display epistasis (van Leeuwen *et al*., 2016). We tested this hypothesis by analyzing the respective genetic crosses. We found that *bim1*Δ *kar9*Δ and *bim1*Δ *cik1*Δ double mutants were viable and did not show aggravated phenotypes relative to the individual mutants (Figure 3I). In contrast, *bim1*Δ was synthetic lethal with mutants involved in nuclear migration, microtubule cross-linking, tension sensing, and centromeric cohesion.

The C-terminus of Bim1 contributes to Cik1-Kar3 function on the mitotic spindle

To define the contributions of Bim1 to spindle function more precisely we augmented the characterization of the *bim1* deletion with an analysis of specific *bim1* mutants. To this end we constructed mutants that interfere with different types of Bim1-based protein interactions. A double point mutation exchanging two conserved residues in the EBH domain (*bim1 Y220A E228A*) is predicted to eliminate all EBH-dependent cargo interactions (Honnappa *et al*., 2009), but should not affect protein dimerization. A deletion of the carboxyterminal five amino acids is predicted to prevent binding of the CAP-Gly domain of Bik1 to Bim1 (Stangier *et al*., 2018). The combination of both mutations is expected to simultaneously prevent both types of interaction (Figure 4A). We tested the designed Bim1 mutants in vitro. Recombinant proteins were well expressed and displayed identical elution profiles during size-exclusion chromatography, indicating identical dimerization status (Supplemental Figure 3A). As expected, the Bim1^{EBH} protein was deficient in Cik1-Kar3 binding, but capable of binding Bik1. In contrast, Bim1$^{\Delta C}$ was able to coelute with Cik1-Kar3, but not with Bik1. The Bim1$^{EBH\Delta C}$ mutant was deficient in both types of interactions. Next, we examined the localization of the major cargoes in these *bim1* mutants in vivo using live cell microscopy (Figure 4B; Supplemental Video 4). As expected, localization of Kar9 on bud-directed astral microtubules was lost in *bim1^{EBH}* and *bim1$^{EBH\Delta C}$* mutants similar to *bim1*Δ, but was unaffected by *bim1$^{\Delta C}$* (Figure 4B). Bik1 localization, on the other hand, was unaffected by *bim1^{EBH}*, but reduced in the *bim1$^{\Delta C}$* mutant (Figure 4C). Interestingly, we found not only that the localization of the main cargo Cik1 to the spindle was dependent on the EBH domain, but also that Cik1 levels were significantly reduced in the *bim1$^{\Delta C}$* mutant (Figure 4, B and D). This effect occurred despite the Bim1$^{\Delta C}$ protein itself being only moderately reduced in its spindle localization (Figure 4B, last row; Supplemental Figure 3B). Overall protein levels of the *bim1* mutants themselves, as well as levels of the main cargoes in these mutants, were unchanged (Supplemental Figure 3, C and D) These results suggest that Bik1 binding to the Bim1 C-terminus contributes to the localization and function of Cik1-Kar3 on the mitotic spindle.

If this is indeed the case, then *bim1$^{\Delta C}$* should have some effect on chromosome segregation. We tested this by characterizing the Bim1 mutant alleles more closely. In bulk growth assays the *bim1$^{\Delta C}$* mutant did not display temperature or benomyl hypersensitivity and it did not exacerbate the effect of *bim1^{EBH}* (Supplemental Figure 4A). In contrast, *bim1^{EBH} and bim1$^{EBH\Delta C}$* behaved similarly to *bim1* deletion. Using live-cell microscopy, we found that *bim1$^{\Delta C}$* did not prolong metaphase duration or have an additive effect on the metaphase duration of *bim1^{EBH}* mutants, which again were the same as for *bim1* deletion (Supplemental Figure 4B). We noticed, however, that the *bim1$^{\Delta C}$* mutant, similarly to *bim1*Δ or *bim1^{EBH}*, displayed an increased accumulation of Ase1 on very short spindles, indicative of problems in spindle organization (Supplemental Figure 4, C and D). Furthermore, in genetic crosses, *bim1$^{\Delta C}$*, just like *bim1^{EBH}* was synthetic lethal with a deletion of the mitotic checkpoint (Supplemental Figure 4E). Taken together, these experiments reveal a role for the C-terminus of Bim1 in Cik1-Kar3 function via binding to Bik1. This role is secondary to the function of the EBH domain, which is mainly responsible for the formation of a Bim1-Cik1-Kar3 complex to which Bik1 can then associate.

Spindle-related Bim1 functions can be provided efficiently by engineered plus-end targeting of Kinesin-14 Cik1-Kar3

Given the similarities between *bim1* and *kar3* deletion, we asked to what extent the spindle phenotypes of *bim1* deletion could be rescued by providing plus-end targeting of Kar3 in the absence of Bim1. We have previously shown that a CH domain fusion to a shortened Cik1 variant lacking the key Bim1 binding motifs (CH-Cik1$^{\Delta 74}$) restores Kar3 plus-end localization and rescues Cik1-Kar3 function in *cik1* deletion cells (Kornakov *et al*., 2020). Here, we have extended this approach by constructing a different chimeric protein, fusing the CH domain of Bim1 (residues 1–133) to full-length Cik1, and then integrating this construct (expressed from a *CIK1* promoter) into *bim1* deletion cells. In essence, this operation generates a cell with only a single Bim1 cargo complex remaining in the nucleus. We then characterized the phenotype of the engineered strain. We found that in serial dilution assays the expression of *CH-Cik1* rescued the temperature, the hydroxyurea, and, to a slightly lesser extent, the benomyl hypersensitivity of the *bim1* deletion (Figure 5A). Expression of *CH-Cik1* was sufficient to shorten the metaphase duration of *bim1*Δ cells back to wild-type timing (31 ± 1 min, 45 ± 1 min, 31 ± 3 min for wild-type, *bim1*Δ, and *CH-Cik1 bim1*Δ, respectively; Figure 5B). Further, we investigated the localization of Ase1 and Bik1 in the *CH-Cik1* strain, as both are altered in the *bim1*Δ background (Figure 1B). We used Ndc80-GFP as a control, since its overall levels at KT clusters did not change upon *bim1* deletion. Relative to *bim1* deletion, expression of *CH-Cik1* decreased the amount of Ase1-GFP and increased the association of Bik1-3xGFP to the metaphase spindle, while the control Ndc80 remained unchanged (Figure 5, C–E). Moreover, *CH-Cik1* almost fully rescued initial metaphase spindle length and partially rescued the maximal metaphase spindle length

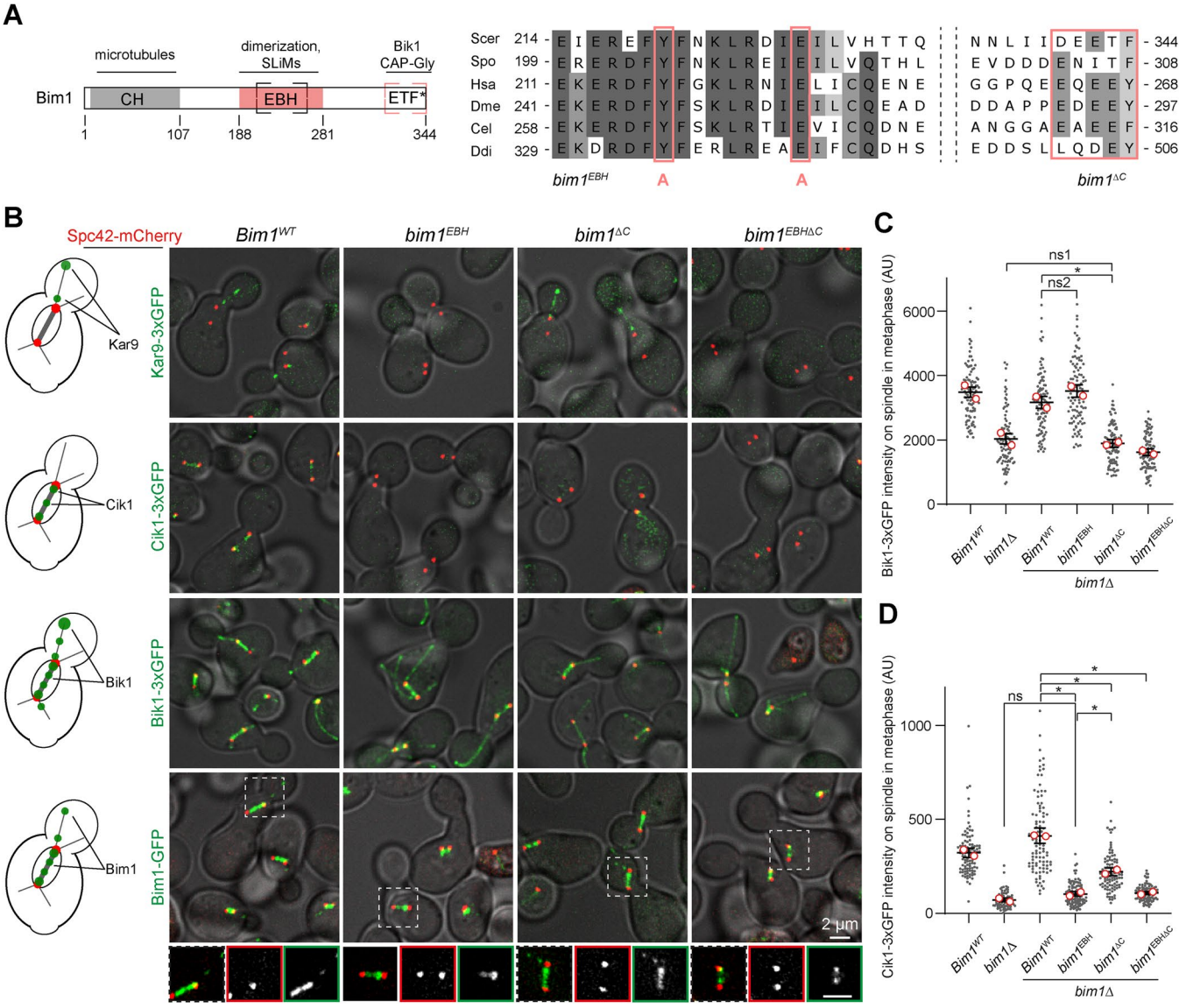

FIGURE 4: The C-terminus of Bim1 contributes to the spindle localization of Cik1. (A) Scheme of Bim1 and indication of point mutations introduced into the EBH domain and the deletion of the C-terminal tail. Multiple sequence alignment prepared in Unipro Ugene shows part of the conserved EBH domain and C-terminus; shaded residues indicate percentage of identity. (B) Fluorescent micrographs of marker proteins Kar9-3xGFP, Cik1-3xGFP, Bik1-GFP in Bim1 wild-type or mutant strains. Last row depicts localization of GFP-tagged Bim1 wild-type or mutants. On the bottom, magnification of the boxed area is shown. From left to right: merged image, red channel, green channel. Strains additionally express Spc42-mCherry. Scale bar, 2 μm. (C) Quantification of Bik1-3xGFP intensity on astral microtubules in different Bim1 mutants. More than 60 cells were analyzed for each condition. Data for wild-type and *bim1*Δ cells are shown for reference and are the same as in Figure 1B. Small dots correspond to individual cells; open red circles represent mean values of repeats. Error bars are mean values with 95% CIs. *, $p < 0.0001$; ns, not significant ($p = 0.9261$); Welch and Brown-Forsythe ANOVA with Games and Howell post-test was used. (D) Quantification of Cik1-3xGFP intensity of spindle microtubules in different *bim1* mutants. One hundred cells were analyzed for each condition. Data for wild-type and *bim1*Δ cells are shown for reference and are the same as in Figure 1B. Small dots correspond to individual cells; open red circles represent mean values of repeats. Error bars are mean values with 95% CIs. *, $p < 0.0001$; ns, not significant ($p = 0.9986$); Welch and Brown-Forsythe ANOVA with Games and Howell post-test was used.

(wild type: 0.92 ± 0.21 μm and 1.98 ± 0.27 μm; *bim1*Δ: 0.67 ± 0.17 μm and 1.48 ± 0.37 μm; *CH-Cik1*: 0.85 ± 0.25 μm and 1.63 ± 0.38 μm; Figure 5, D–F). Overall, *CH-Cik1* improved metaphase spindle organization, but the cells retained a characteristic of the *bim1* deletion in the cytoplasm, displaying high levels of Bik1 on long astral microtubules (Figure 5C). In genetic crosses the *CH-Cik1* chimera fully rescued the lethality of the *bim1*Δ *ase1*Δ and *bim1*Δ *slk19*Δ double mutants. Remarkably, even the lethality of *bim1*Δ in cells lacking the mitotic checkpoint (*mad1*Δ) was partially rescued by the *CH-Cik1* fusion, as corresponding spores were viable, albeit small (Figure 5H). In contrast, the *CH-Cik1* chimera was unable to rescue the lethality of *bim1*Δ mutants in combination with mutants in the nuclear migration pathway (*bik1*Δ or *jnm1*Δ), or in tension sensing and centromeric cohesion (*chl4*Δ; Figure 6H). We have previously

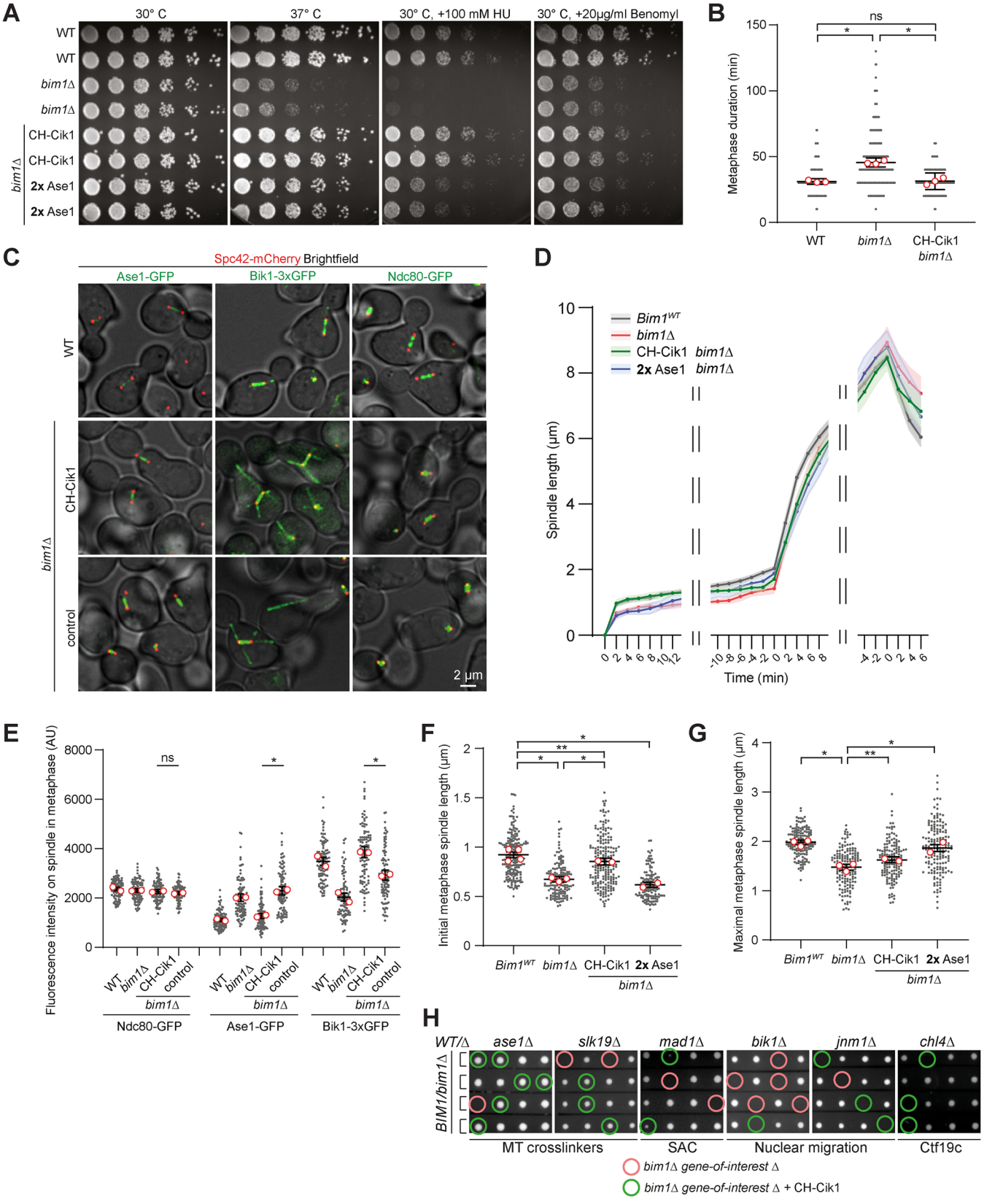

FIGURE 5: Expression of CH-Cik1 or increased dosage of the cross-linker Ase1/PRC1 can compensate for lack of Bim1 in the nucleus. (A) Serial dilution assay testing growth at 30°C, at 37°C, or at 30°C in the presence of 100 mM hydroxyurea or 20 µg/ml benomyl. Plates were photographed after 2.5 d. Note the rescue of temperature and hydroxyurea sensitivity and partial rescue of benomyl sensitivity of a *bim1*Δ mutant by expression of the CH-Cik1 fusion. (B) Quantification of metaphase duration in wild-type cells, *bim1*Δ cells, or cells expressing a chimeric CH-Cik1 fusion protein in *bim1*Δ. Three hundred cells were analyzed for each condition. Small dots correspond to individual cells; open

shown that the phenotype of Bim1-binding deficient Cik1 mutants can be rescued by fusing the CH-domain to this Cik1 mutant (*cik1-Δ74*). The experiments in this study extend those findings and show that a *CH-Cik1* fusion is even able to compensate to a significant degree for a complete absence of Bim1, at least with regards to nuclear spindle functions. This reinforces the notion that the kinesin-14 Cik1-Kar3 is a key Bim1 cargo in the nucleus.

Increased dosage of Ase1 can partially rescue the defects of a *bim1*Δ mutant in mitosis

As an alternative strategy, we tested to what extent elevated expression of the cross-linker Ase1 may suppress the *bim1* deletion phenotype. This experiment was based on the observation that *bim1* deletion cells recruit increased amounts of Ase1 to the metaphase spindle and that these cells require Ase1 for survival. We constructed a series of strains expressing an extra copy of Ase1-GFP under different constitutive promoters of increasing strength (p1 to p5, Supplemental Video 3). While very high overexpression of Ase1 was lethal (unpublished data), moderate expression levels showed a dose-dependent rescue of the temperature sensitivity of the *bim1*Δ mutant (Supplemental Figure 5A). Surprisingly, a single extra copy of Ase1 (*2xAse1*) expressed from its native promoter already provided a decent rescue of *bim1*Δ, albeit not as efficiently as *CH-Cik1* regarding benomyl and hydroxyurea hypersensitivity (Figure 5A). Exogenously expressed Ase1 displayed a level and kinetics of localization similar to those for the endogenous protein, indicating that binding sites for Ase1 are not a limiting factor on the budding yeast spindle (Supplemental Figure 5B). Quantification of metaphase spindle elongation showed that elevated expression of Ase1 (*2xAse1*) was unable to rescue the decreased initial metaphase spindle length of *bim1*Δ cells (Figure 5F), but efficiently restored maximal metaphase spindle length (0.62 ± 0.15 µm and 1.86 ± 0.48 µm; Figure 5, E–G). These findings indicate that expression of CH-Cik1 or increased dosage of Ase1 suppresses different aspects of the *bim1* deletion phenotype. This may reflect distinct roles of Bim1-Cik1-Kar3 in early cross-linking and efficient chromosome biorientation, while late cross-linking mediated by Ase1 is required for the development of full spindle length.

Spindle orientation and nuclear migration in the absence of Bim1 require Bik1

Having characterized the mitotic spindle phenotype, we next analyzed the consequences of a *bim1* deletion in the cytoplasm more closely. Previous work has established two parallel pathways that yeast cells employ to orient and position the nucleus in mitosis. Bim1-Kar9 operates in early mitosis and orients the nucleus along actin cables by linking microtubule plus-ends to the Myosin V motor Myo2 (Beach *et al.*, 2000; Yin *et al.*, 2000; Hwang *et al.*, 2003; Liakopoulos *et al.*, 2003). A second pathway relies on dynein–dynactin pulling on cortical microtubules to promote nuclear migration into the bud neck and spindle elongation into the daughter cell in late metaphase and anaphase (Li *et al.*, 1993; Yeh *et al.*, 1995). Cells can survive with either pathway alone, but simultaneous deletion of both pathways is lethal (Miller and Rose, 1998).

To characterize the cytoplasmic events that occur in the absence of Bim1, we measured the parameters of spindle orientation and nuclear migration in wild-type and *bim1*Δ and in the deletions of its two main cargoes, Kar9 and Kar3. To quantify the phenotypes, we measured the distance between the spindle pole body and the bud-neck axis and evaluated nuclear migration across the bud neck two frames (4 min) after anaphase onset (Figure 6A). As expected, we found that *bim1*Δ and *kar9*Δ cells display spindle positioning defects, characterized by an increased distance between SPB and bud neck on preanaphase spindles (1.11 ± 0.96 µm and 2.27 ± 1.24 µm, compared with 0.58 ± 0.46 µm in wild-type cells; Figure 6B). Despite Bim1 and Kar9 localization on astral microtubules being codependent (see Figure 3D), we found that both spindle orientation and nuclear migration defects were more pronounced in *kar9*Δ than in *bim1*Δ (Figure 6, B and C). To better understand why *bim1*Δ cells have comparatively mild spindle orientation defects, we analyzed additional aspects of this pathway. We measured that *bim1*Δ cells had longer astral microtubules than wild-type cells (4.28 ± 1.2 µm and 2.05 ± 0.72 µm, correspondingly; Figure 6, D and F) and our previous analysis had indicated that these long microtubules are strongly decorated by Bik1 (Figure 1C). Bik1 is part of the dynein–dynactin pathway (Miller *et al.*, 1998) and forms a complex with the plus end–directed kinesin Kip2 (Carvalho *et al.*, 2004), which has microtubule

red circles represent mean values of three biological repeats. Error bars are mean values with 95% CIs. *, $p = 0.0001$; ns, not significant ($p = 0.9893$); one-way ANOVA with Tukey's post-test was used. (C) Merged images of brightfield and fluorescent microscopy of the marker proteins Ase1-GFP, Bik1-3xGFP, and Ndc80-GFP in wild-type cells or in *bim1*Δ cells with an integrated CH-Cik1 fusion gene versus a control. Scale bar 2 µm. (D) Spindle elongation kinetics of the indicated strains. Twenty-five cells were analyzed for CH-Cik1 and control strains. Data for wild-type and *bim1*Δ cells are shown for reference and are the same as in Figure 2C. Curves show mean values with 95% CIs. Breaks in the graph correct for differences in mitotic timing. (E) Quantification of fluorescence intensity on metaphase spindle of marker proteins Ndc80-GFP, Ase1-GFP, and Bik1-3xGFP in the indicated strain backgrounds. One hundred cells were analyzed for CH-Cik1 and control strains for each condition. Small dots correspond to individual cells; open red circles represent mean values of repeats. Data for wild-type and *bim1*Δ cells are shown for reference and are the same as in Figure 1B. Error bars are mean values with 95% CIs. *, $p < 0.0001$; ns, not significant ($p = 0.2038$); unpaired two-tailed Student's *t* test was used. (F) Quantification of initial metaphase spindle length of the indicated strains. Two hundred cells were analyzed for CH-Cik1 and 130 cells for 2x Ase1 strains; data for wild-type and *bim1*Δ cells are shown for reference and are the same as in Figure 2E. Small dots correspond to individual cells; open red circles represent mean values of repeats. Error bars are mean values with 95% CIs. **, $p < 0.0001$; *, $p = 0.0152$; Welch and Brown-Forsythe ANOVA with Games and Howell post-test was used. (G) Quantification of maximal metaphase spindle length of the indicated strains. Seventy-five cells were analyzed for CH-Cik1 and 100 cells for 2x Ase1 strains; data for wild-type and *bim1*Δ cells are shown for reference and are the same as in Figure 2E. Small dots correspond to individual cells; open red circles represent mean values of repeats. Error bars are mean values with 95% CIs. **, $p < 0.0001$; *, $p = 0.0045$; Welch and Brown-Forsythe ANOVA with Games and Howell post-test was used. (H) Heterozygous diploid dissection of different gene deletions in a *bim1*Δ background expressing CH-Cik1 fusion. Four spores of a tetrad are displayed horizontally. The indicated genotypes are marked by circles: red and green circles compare growth of the respective double mutant in the absence or presence of the CH-Cik1 fusion, respectively. Plates were photographed after 2 d.

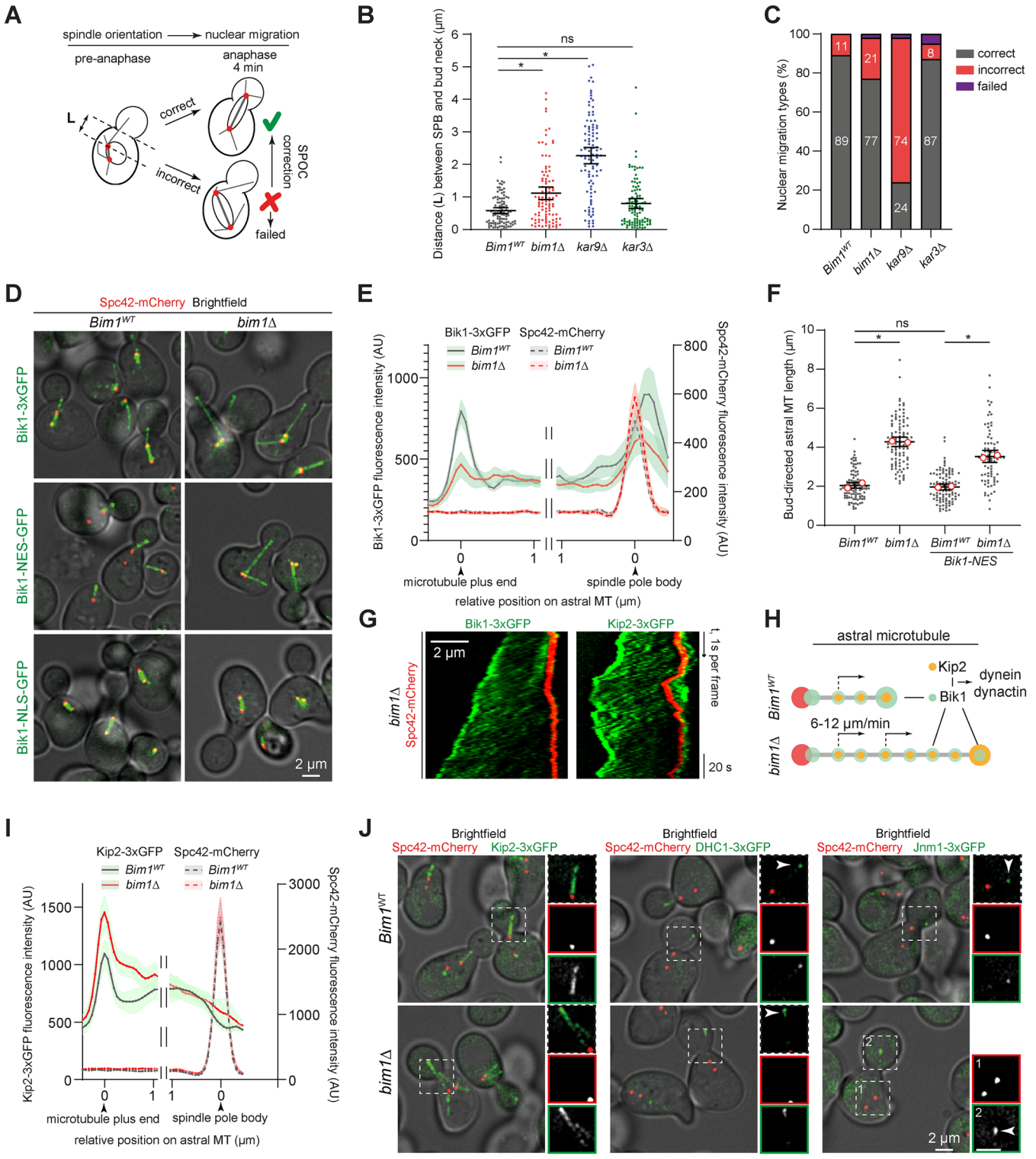

FIGURE 6: Nuclear migration in the absence of Bim1 requires cytoplasmic Bik1. (A) Scheme for scoring spindle orientation and nuclear migration defects. L describes the distance between the bud-proximal spindle pole body and the bud-neck axis; nuclear migration was examined two frames (4 min) after anaphase spindle elongation. (B) Quantification of the distance between the bud-proximal spindle pole body and the bud-neck axis in different mutants. One hundred cells were analyzed for each condition. Small dots correspond to individual cells. Error bars are mean values with 95% CIs. *, $p < 0.0001$; ns, not significant ($p = 0.0866$); Welch and Brown-Forsythe ANOVA with Games and Howell post-test was used. Note the difference between the severity of *bim1*Δ and *kar9*Δ phenotypes. (C) Nuclear migration categories of wild-type cells and different mutants. Two repeats of 100 cells each were quantified; average values are shown. Category "Failed" indicates that anaphase spindles remained completely in the mother cell. (D) Live-cell microscopy of Bik1-3xGFP in wild-type form, or directed to cytoplasm or nucleus via inclusion of an NES or NLS, respectively. Imaging was performed on a wild-type or *bim1*Δ background. Spindle pole bodies are labeled with

polymerase activity in vitro (Hibbel *et al.*, 2015) and in vivo (Chen *et al.*, 2019). Long astral microtubules can interact with the bud cortex and initiate pulling events to move the nucleus (Adames and Cooper, 2000; Omer *et al.*, 2018). We therefore predicted that Bik1 would be needed specifically in the cytoplasm of *bim1* deletion cells to support nuclear migration. To test this directly, we constructed GFP-tagged Bik1 variants that were targeted to the nucleus or the cytoplasm via the inclusion of a nuclear localization signal (*Bik1-NLS*) or a nuclear export signal (*Bik1-NES*), respectively (Figure 6D). In agreement with our prediction, *Bik1-NLS*, lacking cytoplasmic localization, aggravated the growth defect of *bim1* deletion mutants in serial dilution assays (Supplemental Figure 6A). The strain displayed slow growth at 30°C and was nearly inviable at 37°C. In contrast, the combination of *Bik1-NES* and *bim1*Δ displayed growth defects similar to those in the *bim1*Δ strain. Thus, Bik1 is specifically required in the cytoplasm of *bim1*Δ cells. We then analyzed the localization of Bik1 more closely. As expected, the intensity of Bik1 on the plus-ends of astral microtubules was reduced in the *bim1* deletion (Figure 6E; Supplemental Figure 6B). Along the lattice, the majority of Bik1 foci displayed plus-end directed motility, comparable to the speed of Kip2 (~6–12 µm/min; (Figure 6G). Interestingly, in contrast to Bik1, Kip2 displayed a prominent enrichment at the plus-ends in *bim1*Δ cells relative to wild-type (Figure 6, I and J; Supplemental Figure 6C). Similarly, the dynein–dynactin complex subunits Dhc1 and Jnm1 showed an enriched level at plus ends, indicating high activity of the dynein–dynactin pathway in the *bim1* deletion cells (Figure 6J; Figure 1B). This was supported by the observation of frequent spindle tumbling in *bim1*Δ cells (Supplemental Movie 1), which can be caused by dynein-dependent forces pulling at cortical sites (Adames and Cooper, 2000; Omer *et al.*, 2018). Overall our observations indicate that the dynein–dynactin pathway is highly active in *bim1* deletion cells and that these cells require cytoplasmic Bik1.

Bim1 deletion mutants lacking Ase1 or Bik1 have distinct terminal phenotypes

Finally, we sought to define the terminal phenotypes of mutants simultaneously lacking Bim1 and either the microtubule cross-linker Ase1 or the CAP-Gly protein Bik1, as deletions of both proteins were synthetic lethal with *bim1*Δ. Our experiments described above allowed us to predict that Ase1 should be required for mitotic spindle function, while Bik1 should be necessary for nuclear migration of *bim1* deletion cells. To test this directly, we combined the *bim1* deletion mutant with auxin-inducible degron alleles of either Bik1 or Ase1. Additionally, these cells expressed Sgo1-GFP as a marker for tension establishment and Spc42-mCherry to monitor spindle size and position. Cells were imaged after release from an α-factor arrest into auxin-containing medium (Figure 7A). Wild-type cells quickly proceeded through metaphase, reached a 1.61 ± 0.31 µm average spindle length, cleared off Sgo1-GFP as cells achieved biorientation, positioned the spindle in the bud neck, and elongated it between mother and bud in anaphase (Figure 7, A–D). Depletion of Bik1 resulted in a mild decrease of metaphase spindle size (1.39 ± 0.27 µm) but neither a delayed metaphase progression nor an activated tension checkpoint. Cells positioned the spindle properly but underwent spindle elongation almost exclusively within the mother cell. They only managed to conclude nuclear migration during a delay in anaphase (Figure 7, A and D). Ase1 depletion led to a strong decrease in metaphase spindle size similar to *bim1*Δ (1.11 ± 0.25 µm and 1.05 ± 0.29 µm, respectively), but in contrast to *bim1*Δ did not cause accumulation of Sgo1-GFP and had no metaphase delay. The combinations of the *bim1*Δ allele with the two different degrons showed distinct phenotypes: Many *Bik1-AID bim1*Δ cells managed to clear Sgo1-GFP from the spindle and initiated anaphase chromosome segregation. Spindle elongation in these cells, however, occurred nearly exclusively in the mother cell (Figure 7, A and D). The spindles of *Ase1-AID bim1*Δ cells, on the other hand, remained very short (0.83 ± 0.24 µm) and were prominently decorated with Sgo1-GFP; these cells did not initiate anaphase during the course of the experiment (Figure 7, A and B). Thus, both double mutants eventually fail to distribute chromosomes between mother and daughter cell, but they do so with distinctly different terminal phenotypes. Overall, this live-cell analysis is in good agreement with the genetic data and indicates the existence of two parallel and partially redundant pathways for spindle assembly/chromosome biorientation in the nucleus (Bim1-Bik1-Cik1-Kar3 and Ase1-Slk19) and for spindle positioning and nuclear migration in the cytoplasm (Bim1-Kar9-Myo2 and Bik1-Kip2-dynein-dynactin).

DISCUSSION

In this study we have comprehensively analyzed the role of the sole EB protein Bim1 in budding yeast mitosis using a combination of quantitative live-cell imaging and genetic analysis of deletion and point mutants. Our experiments allow us to unify previous observations into a more comprehensive picture of Bim1-dependent and -independent processes during mitosis, and they help to explain how cells organize a microtubule cytoskeleton in the absence of an EB protein.

Defining a minimal set of Bim1 cargo complexes required for efficient mitosis in budding yeast

Successful chromosome segregation in the closed mitosis of budding yeast requires two microtubule-based processes:

Spc42-mCherry. Scale bar, 2 µm. (E) Intensity profiles of Bik1-3xGFP along astral microtubules in wild-type or *bim1*Δ cells. Spc42-mCherry intensity profile is displayed for reference. Break in the graph corrects for different microtubule lengths. Thirty wild-type and 25 *bim1*Δ cells were analyzed. Curves show mean values with 95% CIs. (F) Bud-directed astral microtubule length in wild-type and different mutants. One hundred cells were analyzed for each condition and 80 *Bik1-NES bim1*Δ cells. Small dots correspond to individual cells; open red circles represent mean values from two repeats. Error bars are mean values with 95% CIs. *, $p < 0.0001$; ns, not significant ($p = 0.8923$); Welch and Brown-Forsythe ANOVA with Games and Howell post-test was used. (G) Kymograph analysis of Bik1-3xGFP and Kip2-3xGFP on long cytoplasmic microtubules in *bim1*Δ strains. Scale bar, 2 µm; time-lapse 1s/frame. Note oblique lines indicating movement of Bik1 and Kip2. (H) Schematic representation of Kip2 and Bik1 on cytoplasmic microtubules. (I) Averaged intensity profiles of Kip2-3xGFP along astral microtubules in wild-type and *bim1*Δ cells. Spc42-Cherry profile is included for reference. Twenty-five wild-type and *bim1*Δ cells were analyzed. Curves show mean values with 95% CIs. Break in the graph corrects for different microtubule lengths. (J) Fluorescence micrographs of dynein–dynactin nuclear migration pathway members Kip2, dynein heavy chain (DHC1), and Jnm1 in wild-type or *bim1*Δ cells. Overview merged with brightfield on the left side. Magnification of the boxed area on the right side: merge, red channel, green channel from top to bottom. Arrowheads point at individual Dhc1 or Jnm1 foci. Scale bar 2 µm.

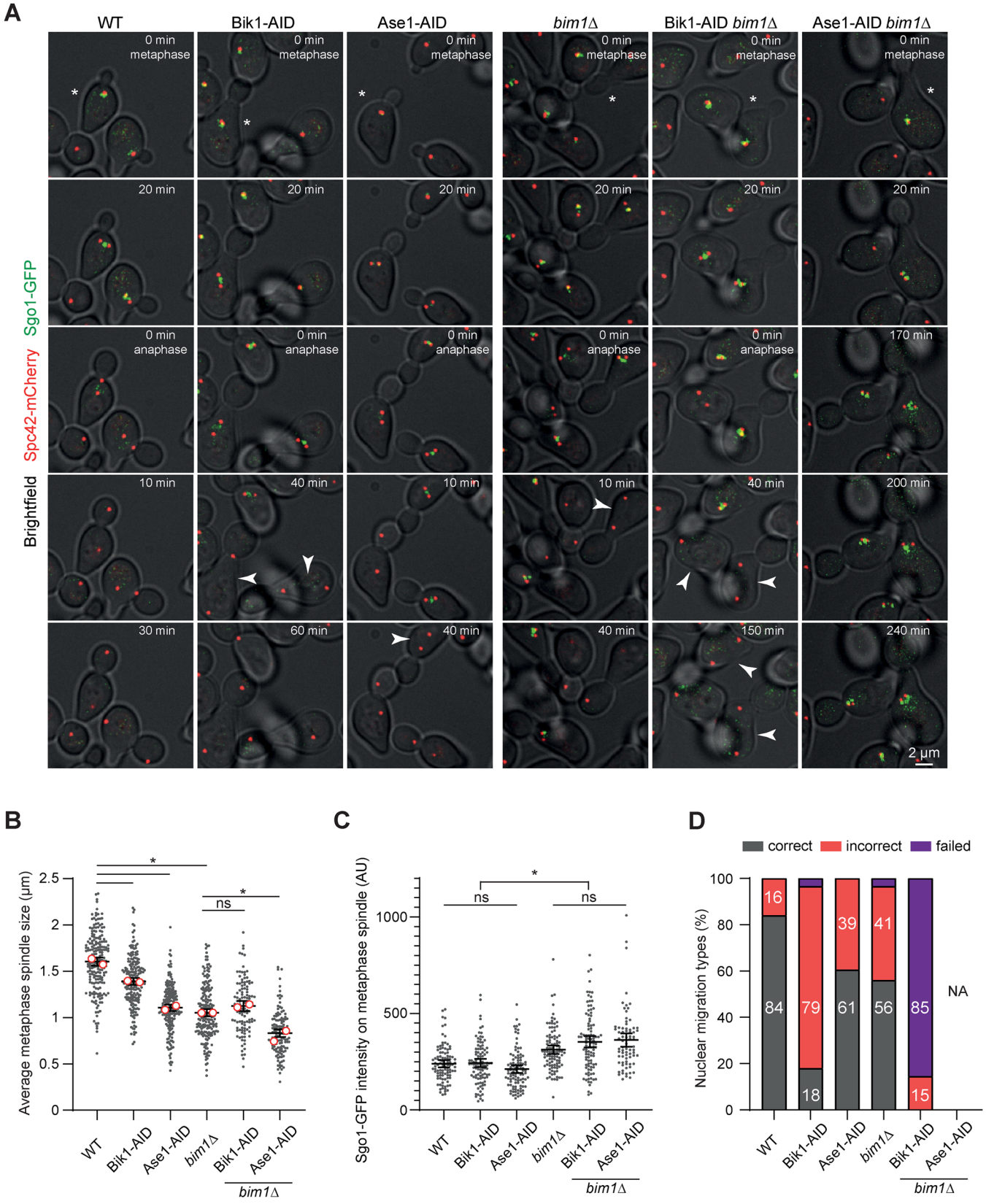

FIGURE 7: Distinct terminal phenotypes of *bim1*Δ cells lacking Ase1 or Bik1. (A) Live-cell microscopy of cells expressing Sgo1-GFP and Spc42-mCherry in the indicated strain backgrounds. Cells were released from α-factor arrest into auxin-containing medium and imaged throughout the cell cycle (time lapse 10 min). Minutes indicate time into metaphase (after initial separation of SPBs) and time after anaphase onset (continued separation of spindle pole bodies) for the cell labeled with the star in the first frame. Arrowheads point at cells elongating anaphase spindles entirely in the mother cell. Scale bar 2 µm. (B) Quantification of average metaphase spindle size (20 min before anaphase) of the

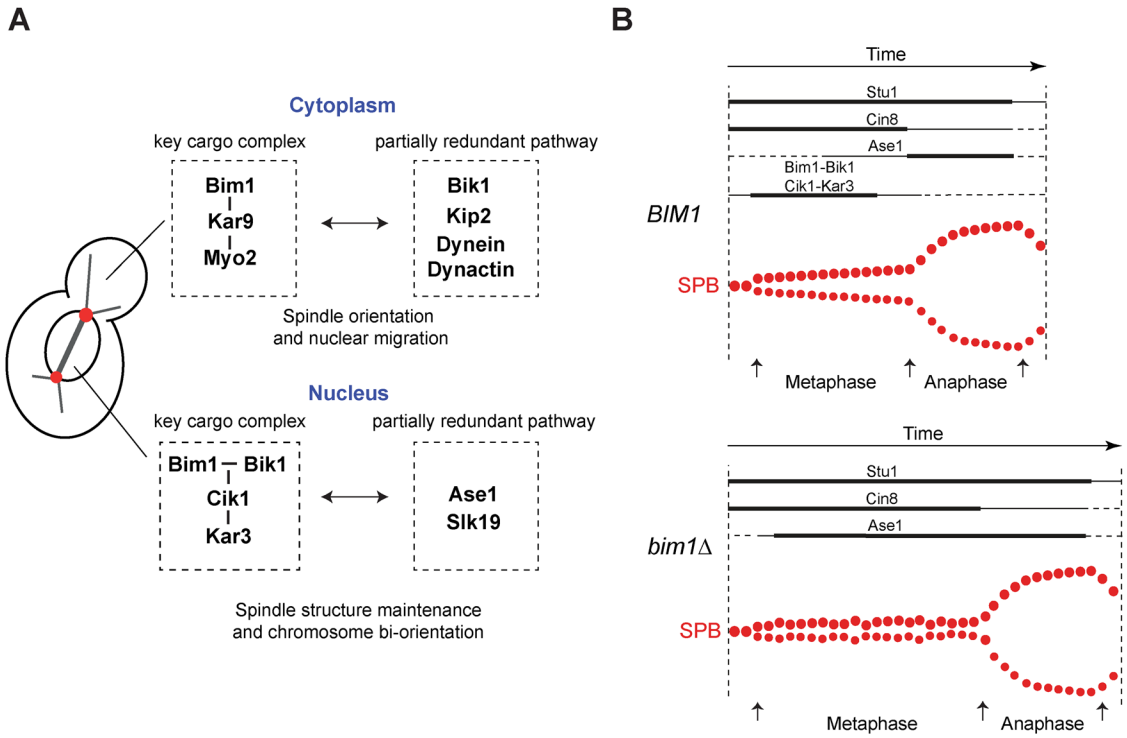

FIGURE 8: Model for functions of key Bim1-cargo complexes. (A) Key Bim1 cargo complexes in cytoplasm and nucleus and parallel pathways required in their absence. In the *bim1*Δ strain, up-regulation of the dynein–dynactin pathway is required for nuclear migration. In the nucleus, increased association of Ase1 or Slk19 is required for metaphase spindle assembly in the absence of Bim1. (B) Schematic representation of spindle assembly and timing of association of microtubule-associated proteins in wild-type and *bim1* deletion cells. See *Discussion* for details.

1) Assembly of a bipolar intranuclear spindle on which sister chromatids biorient and are then separated as the spindle elongates in anaphase. 2) Positioning of the yeast nucleus along the bud-neck axis so that the elongating spindle distributes one set of sister chromatids into the mother and daughter cell. Our analysis indicates that Bim1 contributes to both of these processes as part of two key protein complexes (Figure 8A): Bim1-Kar9-Myo2 in the cytoplasm and Bim1-Bik1-Cik1-Kar3 in the nucleus. These complexes differ from other Bim1 interaction partners in several features: Kar9 and Cik1-Kar3 both strictly require Bim1 for microtubule localization, as judged by live-cell microscopy. This behavior is characteristic, as none of the other 20 tested GFP fusions were as severely affected by the *bim1* deletion. Bim1 and Kar9 mutually depend on each other for localization to cytoplasmic microtubules. In the nucleus, Bim1 is able to localize to the spindle in the absence of Cik1 or Kar3, but the organization of the resulting spindles is as severely impaired as in the *bim1*Δ strains. It is noteworthy that formation of both of these Bim1-cargo complexes not only depends on canonical SxIP motifs, but also involves non-SxIP motifs (LxxPTPh in the case of Kar9 and KLTF-ELN in the case of Cik1-Kar3) in combination with SxIP motifs. Biochemical experiments suggest that the resulting binding mode allows the formation of particularly stable Bim1-cargo complexes (Kornakov *et al.*, 2020; Kumar *et al.*, 2021). The notion that Bim1 executes its cellular functions as part of these stable complexes is supported by our observation that the *bim1*^{EBH} mutant behaves very similar to the *bim1* deletion in our analysis. Thus, microtubule plus-end binding by Bim1 itself contributes little to overall microtubule regulation in cells, and instead Bim1 executes its functions as part of stable cargo complexes.

indicated strains. Number of cells analyzed for every condition: 200 wild-type, 200 *Bik1-AID*, 200 *Ase1-AID*, 200 *bim1*Δ, 110 *Bik1-AID bim1*Δ, 127 *Ase1-AID bim1*Δ. Small dots correspond to individual cells; open red circles represent mean values from two repeats. Error bars are mean values with 95% CIs. *, $p < 0.0001$; ns, not significant ($p = 0.2534$); Welch and Brown-Forsythe ANOVA with Games and Howell post-test was used. Note that *bim1*Δ *Ase1-AID* cells have shortened metaphase spindles relative to *bim1*Δ or *Ase1-AID* alone. (C) Quantification of Sgo1-GFP intensity on metaphase spindles (within 10 min after SPB separation) in the indicated strains. One hundred cells were analyzed for each condition, with the exception of 76 *Ase1-AID bim1*Δ cells. Small dots correspond to individual cells. Error bars are mean values with 95% CIs. *, $p < 0.0001$; ns, not significant; Welch and Brown-Forsythe ANOVA with Games and Howell post-test was used. (D) Quantification of nuclear migration phenotypes. "Incorrect" indicates initial anaphase spindle elongation in the mother cell, which is later corrected; "failed" indicates anaphase spindles that stay in the mother cell. NA: not applicable, since the phenotype is scored relative to anaphase onset and *Ase1-AID bim1*Δ cells do not progress past metaphase. Two repeats of 100 cells each were quantified; average values are shown.

Characteristics of Bim1-dependent spindle phenotypes in budding yeast

The experiments presented in this study have allowed us to better define the phenotypic hallmarks of the *bim1* deletion regarding mitotic spindle function. The phenotype is characterized by a premature and excessive Ase1 recruitment to an overall shorter spindle and by persistent Sgo1 localization. Ase1/PRC1 proteins are known to preferentially cross-link antiparallel microtubule bundles both in vitro and in vivo (Subramanian *et al.*, 2010); therefore we speculate that *bim1*Δ mutants may have more extended antiparallel overlap zones during early spindle assembly than wild-type cells. In budding yeast 32 out of ~40 nuclear microtubules are connected to kinetochores and have a short length of ~340 nm (Winey *et al.*, 1995). One possibility is that *bim1*Δ cells (and therefore cells that lack the Bim1-Bik1-Cik1-Kar3 complex) have a defect in the control of kinetochore microtubule length and more microtubules cross the spindle equator to the opposite kinetochore cluster (Supplemental Figure 2F). A similar activity has been proposed for the kinesin-5 Cin8 (Gardner *et al.*, 2008), and in vitro experiments have demonstrated that EB–kinesin-14 complexes can organize microtubules (Molodtsov *et al.*, 2016) and directly control microtubule plus-end dynamics (Ogren *et al.*, 2022). This would also be consistent with the reported phenotypes of a *cik1* deletion (Hepperla *et al.*, 2014) and may explain why *cik1* loss-of-function mutants predispose cells to form syntelic kinetochore attachments (Jin *et al.*, 2012) which fail to establish tension. Consistent with Bik1 being part of this complex, the removal of Bik1 from the nucleus causes defects in chromosome congression (Julner *et al.*, 2022). Based on our analysis of the relative timing of spindle association, we propose that Bim1-Bik1 in a complex with its cargo Cik1-Kar3 works after initial bipolar spindle formation but before late metaphase and is critical for sister chromatid biorientation (Figure 8B). Ase1, on the other hand, is recruited later, stabilizes the antiparallel overlap zone of interpolar microtubules, and is required for maturation of the metaphase spindle to its full preanaphase length. Our data also indicate that the decrease in metaphase spindle size in *bim1*Δ cells is likely not the key reason for a delay in metaphase progression and chromosome biorientation. Indeed, even nascent bipolar spindles have a length of ~0.9 µm that in principle should allow them to establish tension between sister chromatids (kinetochore microtubule length is ~340 nm). We show that the *ase1* depletion affects spindle length as severely as *bim1*Δ, but has little effect on Sgo1 level and metaphase progression because chromosome biorientation is achieved largely before Ase1 recruitment in late metaphase. Ase1 can only partially substitute for nuclear Bim1 functions, because *2xAse1 bim1*Δ cells still have an increased metaphase duration, indicating that they are not as effective in achieving biorientation as wild-type cells.

Rescuing Bim1-dependent spindle phenotypes with a *CH-Cik1* fusion

A surprising finding from our analysis is that despite many potential binding partners in yeast, the spindle-related phenotypes of a *bim1* deletion can be efficiently rescued by providing a single Bim1 cargo—the kinesin-14 motor Kar3 in the form of a chimeric *CH-Cik1* fusion protein. In particular, our analysis indicates that the *CH-Cik1* fusion rescues the increased metaphase duration of a *bim1* deletion strain, restores wild-type initial metaphase spindle length, decreases the amount of Ase1 on the metaphase spindle (indicative of normal spindle organization), and reestablishes the organization of kinetochore clusters. There are, however, indications that the *CH-Cik1 bim1*Δ strain does not fully behave like a wild type. As it lacks Bim1-Kar9 complexes in the cytoplasm, it has a spindle-positioning defect. This may partly explain the incomplete rescue of the *bim1*Δ *mad1*Δ strain. Also, the double mutant *bim1*Δ *chl4*Δ remains inviable even upon expression of *CH-Cik1*. Perhaps this chimera is very effective in providing efficient spindle organization, indicated by its ability to rescue *bim1*Δ *ase1*Δ or *bim1*Δ *slk19*Δ double mutants, but cannot fully compensate for Bim1's roles in outer kinetochore function or tension-dependent sister chromatid biorientation. An important aspect in which *CH-Cik1* differs from the authentic Bim1-Cik1-Kar3 complex is that it lacks the carboxy terminus of Bim1 and therefore cannot directly bind Bik1. We have shown in this study that the C-terminus of Bim1 contributes to the localization and function of Bim1-Cik1-Kar3. Future experiments will have to relate these observations to the precise molecular functions of Bim1-Cik1-Kar3 and ask how inclusion of Bik1 may modulate specific aspects of these activities.

Differential contributions of Bim1 and Bik1 to spindle orientation pathways

Our observations regarding the effect of *bim1* deletion on cytoplasmic microtubules are in full agreement with the established view of two partially redundant pathways for spindle orientation, only one of which depends on Bim1 by direct binding to Kar9 (Miller *et al.*, 2000). This indicates that in vitro reconstitution experiments that have employed Bim1 to fully reconstitute the Kip2-dependent loading of the dynein–dynactin complex to microtubule-plus ends (Roberts *et al.*, 2014) do not reflect a situation that occurs in these *bim1* deletion cells.

In our experiments we find some indications for an up-regulation of the dynein–dynactin pathway in the *bim1* deletion cells, based on the increased plus-end localization of Kip2 and dynein–dynactin components relative to wild-type cells. For nuclear migration to occur efficiently, the dynein–dynactin complex must be enriched at the plus-ends of cytoplasmic microtubules (Markus and Lee, 2011), contrary to its intrinsic minus end–directed motility (Reck-Peterson *et al.*, 2006). How increased plus-end recruitment of these factors could be accomplished in *bim1* deletion cells and whether up-regulation is really required for nuclear migration remain unclear at this point. In line with previous observations, we find that Bik1 is an important component of the dynein–dynactin pathway. Notably, our acute depletion experiment shows that cells simultaneously lacking Bim1 and Bik1 can form a functional mitotic spindle, but fail to migrate this spindle into the daughter cell. One aspect of how Bik1 contributes to the dynein–dynactin pathway is likely via its interaction with Kip2, but how this occurs mechanistically remains to be established. Kip2 loading is thought to occur at the spindle pole body (Chen *et al.*, 2019), and maybe Bik1 helps Kip2 to reach the plus-end of the very long astral microtubules of *bim1* deletion cells. However, while Kip2 is enriched at plus-ends in *bim1*-deleted cells, the opposite is observed for Bik1. These observations hint that a Kip2-Bik1 complex may not be constitutively present, and perhaps Bik1 dissociates once Kip2 has arrived at the plus-end. Besides, the Kip2-Bik1 pathway is only partially responsible for dynein–dynactin enrichment at plus-ends (Markus *et al.*, 2009), suggesting that the observed enrichment in our *bim1* deletion cells could also be accomplished by different means.

Collectively, our observations in this study reinforce the notion that multiple redundant mechanisms ensure the robustness of spindle assembly and positioning. While the stereotypic construction of the yeast spindle allows a detailed quantification of spindle parameters, a current experimental limitation is that its small size prevents a more precise definition of phenotypes by light microscopy. In the future, cryo-EM tomography in cells, coupled with acute genetic

perturbations and biochemically defined mutants, promises to reveal further insights into the mechanisms by which Bim1-cargo complexes contribute to specific aspects of spindle assembly and function.

Our study highlights the notion that a lack of EB has similar overall consequences on microtubule organization in different systems. Similarly to our findings in budding yeast, acute photoinactivation of EB in human cells leads to a shortening of the metaphase spindle, while anaphase phenotypes are comparatively minor (Dema *et al.*, 2022). Similar effects on spindle length have been reported upon EB RNAi in *Drosophila* cells (Goshima *et al.*, 2007; Li *et al.*, 2011). An increase in astral microtubule length, similar to the effects of a *bim1*Δ, has also been reported as a consequence of EB inactivation in human cells (Dema *et al.*, 2022). In this case, a lack of EB-Kif18B complexes is responsible for the impaired astral microtubule length control. Thus, even though overall consequences of EB loss of function may be similar, they can involve different EB-cargo complexes in different systems.

MATERIALS AND METHODS

Request a protocol through *Bio-protocol*.

Yeast genetics

All strains presented in this study are part of the NKY collection. Most strains were derived by modification of the diploid strain NKY982-2 (MATa/MATα ADE2/ADE2 lys2-801/lys2-801 leu2-3,112/leu2-3,112 Spc42-mCherry::HIS3/SPC42 his3Δ200/his3Δ200 ura3::pGAL-osTIR::URA3/ura3::pGAL-osTIR::URA3 bim1Δ::hphNT1/BIM1), which is a progeny of DDY1102 in the S288c background. One clone of one repeat of every strain used in this study is listed in Supplemental Table S5. Genetic modifications were generated by standard methods (Longtine *et al.*, 1998; Janke *et al.*, 2004) and introduced into yeast using LiAc transformation (Schiestl and Gietz, 1989).

Growth conditions

Yeast was maintained in YEPD medium at 30°C unless otherwise stated. For protein depletion experiments, yeast was grown in YEP medium/plates with raffinose and galactose (2% + 2%) as a sugar source at 30°C. The following antibiotics were used for selection of desired modifications: G418, Nourseothricin (ClonNAT), Hygromycin B. Auxotrophy selection markers were leucine, uracil, and histidine.

Strain construction

After modification of a diploid strain for an antibiotic selection, yeast was first incubated on a YEPD plate and allowed to grow overnight. The next day the plate was replicated on desired selection media and allowed to grow for 2 d until single colonies ~3 mm in size were visible. Typically plates had 50–100 colonies; 8–16 of them were restreaked on a selection plate to confirm resistance. Clones were checked for successful integration by PCRs using gene-specific and resistance cassette primers. For integrations of fluorescent protein tags, the presence of signal was additionally checked at the microscope. Clones were assayed for fitness compared with a parental strain using spot assays. A further two clones were processed for sporulation and tetrad dissection. Twelve tetrads from every clone were genotyped by spotting on testing plates. For chosen spores, tetrads of origin were analyzed for 2–2 segregation of markers by PCR to avoid aneuploidies. Gene deletions were confirmed by PCRs for the absence of wild-type gene and presence of selection marker at correct genomic loci. Functionality of gene tagging was evaluated by comparing growth in wild-type and *bim1*Δ genetic backgrounds with that in corresponding untagged versions. For the experiment, spores were taken directly from dissection plates and were allowed to grow in YEPD overnight. Different clones that originated from the same diploid transformation were considered technical repeats. Transformations performed independently on different days were counted as biological repeats.

Conditional protein depletion by the AID system

The ubiquitin ligase osTIR1 was integrated into the URA3 locus under the control of a galactose-inducible promoter (Nishimura *et al.*, 2009). A synthetic analog of auxin NAA was used at a concentration of 1 mM to induce depletion. Below the preparation of NAA for the experiment is briefly described. A 1-M NAA stock was derived by dissolving NAA in DMSO and further sterile-filtered using a 0.2-µm pore size filter. Aliquots were stored protected from light at -20°C until usage. Before the experiment, an aliquot was thawed and diluted 10-fold in DMSO. To neutralize pH, an equal volume of 0.1 M NaOH was added to the solution.

Western blot sample preparation

Yeast cell extracts were prepared using alkaline treatment as described before (Kushnirov, 2000). Briefly, an equivalent of 2 OD_{600} of exponentially growing cells was harvested, washed with H_2O, and resuspended in 200 µl of 0.1 M NaOH. After 5 min incubation at room temperature, cells were centrifuged again. The pellet was resuspended in 50 µl 1x SDS sample buffer and boiled for 5 min. A quantity of 8–10 µl of lysate was loaded per gel lane.

Used antibodies and visualization

α-GFP (*Roche*, from mouse) 1:1000; α-myc (*Covance*, 9E10 from mouse) 1:1000; α-tubulin-HRP 1:1000 (*Santa Cruz,* from rat); HRP-coupled α-mouse (*GE Healthcare*) 1:10,000. All antibodies were diluted in 5% (wt/vol) milk in TBST. For visualization, Amersham ECL Prime Western Blotting Detection Reagent (GE Healthcare) was used. Images were acquired by an Amersham Imager 600 (GE Healthcare).

Plasmid construction

All plasmids generated and used are listed in Supplemental Table S2.

Recombinant protein work and biochemistry

Protein expression, purification, size-exclusion chromatography, and quantitative pulldowns were performed as described by Kornakov *et al.* (2020) except for the following modifications. Quantitative pulldowns were made in buffer containing 300 mM NaCl to better reflect physiological ion strength in yeast (van Eunen *et al.*, 2010). Imidazole concentration was reduced from 10 to 5 mM to prevent leakage of bound proteins from TALON beads.

Serial dilution spot assays

Yeast strains were grown overnight (16–18 h) in YEPD media. Aliquots were spun down, washed two times with sugar-free minimal medium, and resuspended in it. serial dilutions (1:4) from a starting OD of 0.2 were prepared in a sterile 96-well plate using minimal medium as a solvent. Yeasts were transferred to the desired plates using a VP407AH 48-pin replicator (V&P Scientific, Inc). Plates were incubated under indicated conditions for 2–2.5 d until colonies of size ~2 mm were visible.

Protein engineering and genetic constructs

Construction of a functional GFP-tagged version of Bim1. A small library of N-, C-, and internally GFP-tagged versions of Bim1 was prepared. GFP was inserted using $(GS)_n$ and $(GA)_n$ flexible

linkers between the Bim1 coding sequence and GFP. Constructs-encoding plasmids were integrated into the LEU2 locus in the heterozygous *BIM1/bim1Δ MAD1/mad1Δ* (NKY1048-1) diploid strain. Functionality was addressed by the ability of GFP-tagged constructs to rescue temperature, hydroxyurea, and benomyl hypersensitivities of *bim1* deletion and by viability in the absence of a functional SAC (*mad1Δ*). Tested constructs displayed a variety of phenotypes and associated defects. The only fully functional version was $Bim1^{WT}$-GFP that contained GFP inserted close to the extreme C-terminus of Bim1 10 amino acids before the stop codon. The sequence of the insertion point is EGEVGVS-$(GA)_5$-GFP-$(GGGS)_2$-NNLIIDEETF*; Bim1 sequences are underlined.

Artificial relocalization of Bik1. To target Bik1 to the nucleus or the cytoplasm, it was modified with NLS-GFP or NES-GFP at its native locus. Constructs used for homologous recombination were prepared using overlapping-extension PCRs. The SV40 NLS (PKKKRKV) or canonical NES (LAEKLAGLDIN) sequences were inserted directly following the Bik1 coding sequence (-NQQFF*) without a linker. Bik1-NES had an exclusively cytoplasmic localization; the Bik1 signal on the mitotic spindle was reduced to background levels. Bik1-NLS had a predominantly nuclear localization. However, a weak signal corresponding to ends of short cytoplasmic microtubules was still detectable, indicating an existence of natural determinants of cytoplasmic localization of Bik1.

Artificial plus-end targeting of Kinesin-14 (CH-Cik1). Kinesin-14 was artificially targeted to the microtubule plus-ends by fusing the CH-domain of Bim1 to the N-terminus of the kinesin-associated protein Cik1. Briefly, amino acids 1–133 of Bim1 were fused to the full coding sequence of Cik1 using a $(GGGS)_2$ linker. The construct contained the 5′UTR of Cik1. The difference from the previously used CH-$Cik1^{\Delta 74}$ version (Kornakov *et al.*, 2020) is that CH-$Cik1^{FL}$ retains a natural NLS and degron sequences located within the Cik1 tail. In our hands it behaves slightly better than CH-$Cik1^{\Delta 74}$ and allows us to release cells from α-factor arrest more efficiently. The CH-domain of Bim1 comprises the N-terminal 133 amino acids.

Constitutive promoter library. A small library of six constitutive promoters of increasing strength was constructed based on a previous analysis (Shaw *et al.*, 2019). Constructs ranged from the weakest promoter, p1, to the strongest, p6 (p1 = pREV1 < p2 = pPSP2 < p3 = pRNR2 < p4 = pRET2 < p5 = pRPL18B < p6 = pCCW12). In our hands p3 provided stronger expression of Ase1-GFP than p4. All promoters were 700 bp in length, besides pPSP2, which was 400 bp.

Live-cell fluorescence microscopy

Microscopy setup. Live-cell microscopy was performed using the DeltaVison Elite widefield microscope system (GE Healthcare) at 30°C. A 100× objective with 1.4 NA (Olympus) and immersion oil with a refractive index of $n = 1.518$ were used. Images were typically acquired by optical axis integration scans over 3 µm width and captured with an sCMOS camera. Images were taken every 10 min, or for higher–time resolution experiments every 2 min. Cells were immobilized on Concanavalin A coated eight- and four-well ibidi glass-bottomed µ-slide 1.5H. All images were deconvolved using SoftWoRx 7 (options: enhanced ratio, aggressive); image analysis was performed using ImageJ/Fiji software.

Quantification of fluorescence intensity. Fluorescence intensity was quantified as a background-corrected area under the curve derived by line scan; line scan was of width 10 pixels across the spindle or a bud-directed astral microtubule. Background was defined for every fluorescence intensity profile by drawing a line under a signal curve connecting regions that are outside of the spindle but still within the cell.

Live-cell imaging preparations. Cells were grown overnight (16–18 h) in YEPD medium at 30°C. In the morning, cultures were diluted 1 to 100 in fresh media and cells were allowed to achieve exponential growth for 2–3 h at 30°C. For protein depletion experiments, cells were grown in YEPRG (2% wt/vol of raffinose and 2% of galactose). Then 0.01 mg/ml α-factor was added for 2 h to arrest cells in a G1-like state. Synchronized cells were spun down; α-factor was washed away with prewarmed medium two times for YEPD cultures and three times for YEPRG cultures. For protein depletion, the last wash contained 1 mM of NAA. After the last wash, cells were resuspended in doTRP minimal medium with a sugar source as desired.

Statistical analysis

Statistical tests and graphs were prepared using Graphpad Prism 8 and 9. Small points on graphs show values of individual cells; large open circles represent means of biological or technical replicates, as indicated. A 95% confidence interval is usually shown. In the text, mean values ±SEM are mentioned. Student's *t* test was used to compare continuous data from two strains. For multiple comparisons Welch and Brown-Forsythe ANOVA with Games and Howell post-test was used to compare pooled data; one-way ANOVA with Tukey's post-test was used to compare data with biological repeats, as indicated.

ACKNOWLEDGMENTS

The authors acknowledge Alexander Dudziak, Christian Cozma, and Jennifer Harris for critical reading of the manuscript and all members of the Westermann laboratory for discussions. Microscopy experiments were carried out with support from the Imaging Center Campus Essen Core Facility (ICCE). The DeltaVision Elite high-resolution microscope was obtained through Deutsche Forschungsgemeinschaft funding (Major Research Instrumentation Programme per Art. 91b GG, INST 20876/275-1). S.W. acknowledges funding by the Deutsche Forschungsgemeinschaft (DFG, German Research Foundation)-SFB1430-Project-ID 424228829.

REFERENCES

Adames NR, Cooper JA (2000). Microtubule interactions with the cell cortex causing nuclear movements in *Saccharomyces cerevisiae*. J Cell Biol 149, 863–874.

Akhmanova A, Steinmetz MO (2008). Tracking the ends: a dynamic protein network controls the fate of microtubule tips. Nat Rev Mol Cell Biol 9, 309–322.

Beach DL, Thibodeaux J, Maddox P, Yeh E, Bloom K (2000). The role of the proteins Kar9 and Myo2 in orienting the mitotic spindle of budding yeast. Curr Biol 10, 1497–1506.

Bieling P, Kandels-Lewis S, Telley IA, van Dijk J, Janke C, Surrey T (2008). CLIP-170 tracks growing microtubule ends by dynamically recognizing composite EB1/tubulin-binding sites. J Cell Biol 183, 1223–1233.

Bieling P, Laan L, Schek H, Munteanu EL, Sandblad L, Dogterom M, Brunner D, Surrey T (2007). Reconstitution of a microtubule plus-end tracking system in vitro. Nature 450, 1100–1105.

Brouhard GJ, Rice LM (2018). Microtubule dynamics: an interplay of biochemistry and mechanics. Nat Rev Mol Cell Biol 19, 451–463.

Buey RM, Sen I, Kortt O, Mohan R, Gfeller D, Veprintsev D, Kretzschmar I, Scheuermann J, Neri D, Zoete V, *et al.* (2012). Sequence determinants of a microtubule tip localization signal (MtLS). J Biol Chem 287, 28227–28242.

Carvalho P, Gupta ML Jr., Hoyt MA, Pellman D (2004). Cell cycle control of kinesin-mediated transport of Bik1 (CLIP-170) regulates microtubule stability and dynein activation. Dev Cell 6, 815–829.
Chen X, Widmer LA, Stangier MM, Steinmetz MO, Stelling J, Barral Y (2019). Remote control of microtubule plus-end dynamics and function from the minus-end. eLife 8, e48627.
Costanzo M, VanderSluis B, Koch EN, Baryshnikova A, Pons C, Tan G, Wang W, Usaj M, Hanchard J, Lee SD, *et al*. (2016). A global genetic interaction network maps a wiring diagram of cellular function. Science 353.
Dema A, van Haren J, Wittmann T (2022). Optogenetic EB1 inactivation shortens metaphase spindles by disrupting cortical force-producing interactions with astral microtubules. Curr Biol 32, 1197–1205.e1194.
Dudziak A, Engelhard L, Bourque C, Klink BU, Rombaut P, Kornakov N, Janen K, Herzog F, Gatsogiannis C, Westermann S (2021). Phospho-regulated Bim1/EB1 interactions trigger Dam1c ring assembly at the budding yeast outer kinetochore. EMBO J 40, e108004.
Estrem C, Moore JK (2019). Astral microtubule forces alter nuclear organization and inhibit DNA repair in budding yeast. Mol Biol Cell 30, 2000–2013.
Fink G, Lowe J (2015). Reconstitution of a prokaryotic minus end-tracking system using TubRC centromeric complexes and tubulin-like protein TubZ filaments. Proc Natl Acad Sci USA 112, E1845–E1850.
Gardner MK, Bouck DC, Paliulis LV, Meehl JB, O'Toole ET, Haase J, Soubry A, Joglekar AP, Winey M, Salmon ED, *et al*. (2008). Chromosome congression by Kinesin-5 motor-mediated disassembly of longer kinetochore microtubules. Cell 135, 894–906.
Goshima G, Wollman R, Goodwin SS, Zhang N, Scholey JM, Vale RD, Stuurman N (2007). Genes required for mitotic spindle assembly in *Drosophila* S2 cells. Science 316, 417–421.
Hepperla AJ, Willey PT, Coombes CE, Schuster BM, Gerami-Nejad M, McClellan M, Mukherjee S, Fox J, Winey M, Odde DJ, *et al*. (2014). Minus-end-directed Kinesin-14 motors align antiparallel microtubules to control metaphase spindle length. Dev Cell 31, 61–72.
Hibbel A, Bogdanova A, Mahamdeh M, Jannasch A, Storch M, Schaffer E, Liakopoulos D, Howard J (2015). Kinesin Kip2 enhances microtubule growth in vitro through length-dependent feedback on polymerization and catastrophe. eLife 4, e10542.
Honnappa S, Gouveia SM, Weisbrich A, Damberger FF, Bhavesh NS, Jawhari H, Grigoriev I, van Rijssel FJ, Buey RM, Lawera A, *et al*. (2009). An EB1-binding motif acts as a microtubule tip localization signal. Cell 138, 366–376.
Hwang E, Kusch J, Barral Y, Huffaker TC (2003). Spindle orientation in *Saccharomyces cerevisiae* depends on the transport of microtubule ends along polarized actin cables. J Cell Biol 161, 483–488.
Indjeian VB, Stern BM, Murray AW (2005). The centromeric protein Sgo1 is required to sense lack of tension on mitotic chromosomes. Science 307, 130–133.
Janke C, Magiera MM, Rathfelder N, Taxis C, Reber S, Maekawa H, Moreno-Borchart A, Doenges G, Schwob E, Schiebel E, Knop M (2004). A versatile toolbox for PCR-based tagging of yeast genes: new fluorescent proteins, more markers and promoter substitution cassettes. Yeast 21, 947–962.
Jiang K, Toedt G, Montenegro Gouveia S, Davey NE, Hua S, van der Vaart B, Grigoriev I, Larsen J, Pedersen LB, Bezstarosti K, *et al*. (2012). A proteome-wide screen for mammalian SxIP motif-containing microtubule plus-end tracking proteins. Curr Biol 22, 1800–1807.
Jin F, Liu H, Li P, Yu HG, Wang Y (2012). Loss of function of the Cik1/Kar3 motor complex results in chromosomes with syntelic attachment that are sensed by the tension checkpoint. PLoS Genet 8, e1002492.
Julner A, Abbasi M, Menendez-Benito V (2022). The microtubule plus-end tracking protein Bik1 is required for chromosome congression. Mol Biol Cell 33, br7.
Kornakov N, Mollers B, Westermann S (2020). The EB1-Kinesin-14 complex is required for efficient metaphase spindle assembly and kinetochore bi-orientation. J Cell Biol 219, e202003072.
Kumar A, Manatschal C, Rai A, Grigoriev I, Degen MS, Jaussi R, Kretzschmar I, Prota AE, Volkmer R, Kammerer RA, *et al*. (2017). Short linear sequence motif LxxPTPh targets diverse proteins to growing microtubule ends. Structure 25, 924–932.e924.
Kumar A, Meier SM, Farcas AM, Manatschal C, Barral Y, Steinmetz MO (2021). Structure and regulation of the microtubule plus-end tracking protein Kar9. Structure 29, 1266–1278.e1264.
Kushnirov VV (2000). Rapid and reliable protein extraction from yeast. Yeast 16, 857–860.
Li W, Miki T, Watanabe T, Kakeno M, Sugiyama I, Kaibuchi K, Goshima G (2011). EB1 promotes microtubule dynamics by recruiting Sentin in *Drosophila* cells. J Cell Biol 193, 973–983.
Li YY, Yeh E, Hays T, Bloom K (1993). Disruption of mitotic spindle orientation in a yeast dynein mutant. Proc Natl Acad Sci USA 90, 10096–10100.
Liakopoulos D, Kusch J, Grava S, Vogel J, Barral Y (2003). Asymmetric loading of Kar9 onto spindle poles and microtubules ensures proper spindle alignment. Cell 112, 561–574.
Longtine MS, McKenzie A 3rd, Demarini DJ, Shah NG, Wach A, Brachat A, Philippsen P, Pringle JR (1998). Additional modules for versatile and economical PCR-based gene deletion and modification in *Saccharomyces cerevisiae*. Yeast 14, 953–961.
Manatschal C, Farcas AM, Degen MS, Bayer M, Kumar A, Landgraf C, Volkmer R, Barral Y, Steinmetz MO (2016). Molecular basis of Kar9-Bim1 complex function during mating and spindle positioning. Mol Biol Cell 27, 3729–3745.
Manning BD, Barrett JG, Wallace JA, Granok H, Snyder M (1999). Differential regulation of the Kar3p kinesin-related protein by two associated proteins, Cik1p and Vik1p. J Cell Biol 144, 1219–1233.
Markus SM, Lee WL (2011). Regulated offloading of cytoplasmic dynein from microtubule plus ends to the cortex. Dev Cell 20, 639–651.
Markus SM, Punch JJ, Lee WL (2009). Motor- and tail-dependent targeting of dynein to microtubule plus ends and the cell cortex. Curr Biol 19, 196–205.
Maurer SP, Fourniol FJ, Bohner G, Moores CA, Surrey T (2012). EBs recognize a nucleotide-dependent structural cap at growing microtubule ends. Cell 149, 371–382.
Mieck C, Molodtsov MI, Drzewicka K, van der Vaart B, Litos G, Schmauss G, Vaziri A, Westermann S (2015). Non-catalytic motor domains enable processive movement and functional diversification of the kinesin-14 Kar3. eLife 4, e04489.
Miller RK, Cheng SC, Rose MD (2000). Bim1p/Yeb1p mediates the Kar9p-dependent cortical attachment of cytoplasmic microtubules. Mol Biol Cell 11, 2949–2959.
Miller RK, Heller KK, Frisen L, Wallack DL, Loayza D, Gammie AE, Rose MD (1998). The kinesin-related proteins, Kip2p and Kip3p, function differently in nuclear migration in yeast. Mol Biol Cell 9, 2051–2068.
Miller RK, Rose MD (1998). Kar9p is a novel cortical protein required for cytoplasmic microtubule orientation in yeast. J Cell Biol 140, 377–390.
Molodtsov MI, Mieck C, Dobbelaere J, Dammermann A, Westermann S, Vaziri A (2016). A force-induced directional switch of a molecular motor enables parallel microtubule bundle formation. Cell 167, 539–552.e514.
Moore JK, D'Silva S, Miller RK (2006). The CLIP-170 homologue Bik1p promotes the phosphorylation and asymmetric localization of Kar9p. Mol Biol Cell 17, 178–191.
Nishimura K, Fukagawa T, Takisawa H, Kakimoto T, Kanemaki M (2009). An auxin-based degron system for the rapid depletion of proteins in nonplant cells. Nat Methodsl 6, 917–922.
Ogren A, Parmar S, Mukherjee S, Gonzalez SJ, Plooster M, McClellan M, Mannava AG, Davidson E, Davis TN, Gardner MK (2022). Kinesin-14 motors participate in a force balance at microtubule plus-ends to regulate dynamic instability. Proc Natl Acad Sci USA 119, e2108046119.
Omer S, Greenberg SR, Lee WL (2018). Cortical dynein pulling mechanism is regulated by differentially targeted attachment molecule Num1. Elife 7, e36745.
Reck-Peterson SL, Yildiz A, Carter AP, Gennerich A, Zhang N, Vale RD (2006). Single-molecule analysis of dynein processivity and stepping behavior. Cell 126, 335–348.
Roberts AJ, Goodman BS, Reck-Peterson SL (2014). Reconstitution of dynein transport to the microtubule plus end by kinesin. Elife 3, e02641.
Schiestl RH, Gietz RD (1989). High efficiency transformation of intact yeast cells using single stranded nucleic acids as a carrier. Curr Genet 16, 339–346.
Schwartz K, Richards K, Botstein D (1997). BIM1 encodes a microtubule-binding protein in yeast. Mol Biol Cell 8, 2677–2691.
Schweiggert J, Panigada D, Tan AN, Liakopoulos D (2016). Kar9 controls the nucleocytoplasmic distribution of yeast EB1. Cell Cycle 15, 2860–2866.
Shaw WM, Yamauchi H, Mead J, Gowers GF, Bell DJ, Oling D, Larsson N, Wigglesworth M, Ladds G, Ellis T (2019). Engineering a model cell for rational tuning of GPCR signaling. Cell 177, 782–796.e727.
Stangier MM, Kumar A, Chen X, Farcas AM, Barral Y, Steinmetz MO (2018). Structure–function relationship of the Bik1-Bim1 complex. Structure 26, 607–618.e604.
Subramanian R, Wilson-Kubalek EM, Arthur CP, Bick MJ, Campbell EA, Darst SA, Milligan RA, Kapoor TM (2010). Insights into antiparallel microtubule crosslinking by PRC1, a conserved nonmotor microtubule binding protein. Cell 142, 433–443.

Tirnauer JS, Canman JC, Salmon ED, Mitchison TJ (2002). EB1 targets to kinetochores with attached, polymerizing microtubules. Mol Biol Cell 13, 4308–4316.
Tong AH, Evangelista M, Parsons AB, Xu H, Bader GD, Page N, Robinson M, Raghibizadeh S, Hogue CW, Bussey H, *et al*. (2001). Systematic genetic analysis with ordered arrays of yeast deletion mutants. Science 294, 2364–2368.
Usaj M, Tan Y, Wang W, VanderSluis B, Zou A, Myers CL, Costanzo M, Andrews B, Boone C (2017). TheCellMap.org: A web-accessible database for visualizing and mining the global yeast genetic interaction network. G3 (Bethesda) 7, 1539–1549.
van der Vaart B, Fischbock J, Mieck C, Pichler P, Mechtler K, Medema RH, Westermann S (2017). TORC1 signaling exerts spatial control over microtubule dynamics by promoting nuclear export of Stu2. J Cell Biol 216, 3471–3484.
van Eunen K, Bouwman J, Daran-Lapujade P, Postmus J, Canelas AB, Mensonides FI, Orij R, Tuzun I, van den Brink J, Smits GJ, *et al*. (2010). Measuring enzyme activities under standardized in vivo-like conditions for systems biology. FEBS J 277, 749–760.
van Leeuwen J, Pons C, Mellor JC, Yamaguchi TN, Friesen H, Koschwanez J, Usaj MM, Pechlaner M, Takar M, Usaj M, *et al*. (2016). Exploring genetic suppression interactions on a global scale. Science 354, aag0839.
Wickstead B, Gull K, Richards TA (2010). Patterns of kinesin evolution reveal a complex ancestral eukaryote with a multifunctional cytoskeleton. BMC Evol Biol 10, 110.
Winey M, Mamay CL, O'Toole ET, Mastronarde DN, Giddings TH Jr., McDonald KL, McIntosh JR (1995). Three-dimensional ultrastructural analysis of the Saccharomyces cerevisiae mitotic spindle. J Cell Biol 129, 1601–1615.
Yeh E, Skibbens RV, Cheng JW, Salmon ED, Bloom K (1995). Spindle dynamics and cell cycle regulation of dynein in the budding yeast, *Saccharomyces cerevisiae*. J Cell Biol 130, 687–700.
Yin H, Pruyne D, Huffaker TC, Bretscher A (2000). Myosin V orientates the mitotic spindle in yeast. Nature 406, 1013–1015.
Yutin N, Koonin EV (2012). Archaeal origin of tubulin. Biol Direct 7, 10.